

Accepted and scheduled for publication in *the Astrophysical Journal*, for April 10, 2007, v 659 1 issue

Power spectra of black holes and neutron stars as a probe of hydrodynamical structure of the source. Diffusion theory and its application to Cyg X-1 and Cyg X-2 X-ray observations

Lev Titarchuk^{1,2,3}, Nikolai Shaposhnikov⁴ and Vadim Arefiev⁵

ABSTRACT

We present a model of Fourier Power Density Spectrum (PDS) formation in accretion powered X-ray binary systems derived from the first principles of the diffusion theory. Timing properties of X-ray emission are considered to be a result of diffusive propagation of the driving perturbations in a bounded medium. We prove that the integrated power of the resulting PDS, P_x is only a small fraction of the integrated power of the driving oscillations, P_{dr} which is distributed over the disk. Furthermore, we demonstrate that the power P_x is inversely proportional to the characteristic frequency of the driving oscillations ν_{dr} which is likely scaled with the frequency of the local gravity waves in the disk (Keplerian frequency). Keeping in mind that ν_{dr} increases towards soft states leads us to conclude that the power P_x declines towards soft states. This dependence $P_x \propto \nu_{dr}^{-1}$ explains the well-known observational phenomenon that the power of the X-ray variability decreases when the source evolves to softer states. The resulting PDS continuum is a sum of two components, a low frequency (LF) component which presumably originates in an extended accretion disk and a high frequency (HF) component which originates in the innermost part of the source [Compton cloud (CC)]. The LF PDS component has a power-law shape with index of 1.0 – 1.5 at higher

¹George Mason University/Center for Earth Observing and Space Research, Fairfax, VA 22030; and US Naval Research Laboratory, Code 7655, Washington, DC 20375-5352; ltitarchuk@ssd5.nrl.navy.mil

²Dipartimento di Fisica, Università di Ferrara, via Saragat 1, I-44100, Ferrara, Italy; titarchuk@fe.infn.it

³Goddard Space Flight Center, NASA, code 661, Greenbelt MD 20771; lev@milkyway.gsfc.nasa.gov

⁴Goddard Space Flight Center, NASA/Universities Space Research Association, code 662, Greenbelt MD 20771; nikolai@milkyway.gsfc.nasa.gov

⁵Space Research Institute (IKI), Russian Academy of Science, Profsoyuznaya 84/32, 117997, Moscow, Russia, gita@hea.iki.rssi.ru

frequencies (“red” noise) and a flat spectrum below a characteristic (break) frequency (“white” noise). This white-red noise (WRN) continuum spectrum holds information about the physical parameters of the bounded extended medium, diffusion time scale and the dependence law of viscosity vs radius. This LF PDS associated with the extended disk dominates in the soft states of the system, while the HF PDS characteristic of innermost CC component is dominant in the low/hard and intermediate states. These PDS LF and HF components directly correspond to the energy spectrum components. Namely: LF WRN is related to thermal emission from an accretion disk, and the HF WRN to the power-law tail, which presents a fraction of the disk emission Comptonized in the Compton cloud. Hence, a change of PDS features correlates with a change of energy spectral features. Analyzing the data for a number of sources we find that the PDS is well represented by a sum of the WRN CC component and the WRN extended disk component. We apply our model of the PDS to a sample of RXTE and EXOSAT timing data from Cyg X-1 and Cyg X-2 which describes adequately the spectral transitions in these sources. The presented PDSs are shown in frequency range from 10^{-8} Hz to 10^2 Hz, i.e. in 10 orders of magnitude range. We offer a method to measure an effective Reynolds number, (Re) [inverse of the disk viscosity (α_{SS})–parameter] using the basic power spectrum parameters, PDS index and characteristic frequencies. Our analysis gives Re in the range of 8 ± 2.5 , or $\alpha_{SS} \sim (\text{Re})^{-1} = 0.14 \pm 0.04$, for the Cyg X-1 and Cyg X-2 CC configurations which are associated with their HF PDS component.

Subject headings: accretion, accretion disks—black hole physics—stars:individual (Cyg X-1), individual (Cyg X-2), individual (GRO J1655-40), individual (XTE 1859+226) :radiation mechanisms: nonthermal—physical data and processes

1. Introduction

In Astronomy, in general the basic question is: what one can learn from the observations confronting a theory derived from the first principles and the main laws of Physics. Particularly, X-ray Astronomy studies the spectral and timing properties of X-ray emission sources. During the last three decades a bulk of observational evidence emerged, showing that black hole X-ray binaries evolves through a set of spectral states (see Remillard & McClintock 2006, and references therein). The basic properties of the X-ray energy spectra in a particular state are determined by a distribution of photons between two major spectral continuum components, i.e. the thermal component which comes from an accretion disk and the power

law, presumably formed by the soft disk photons upscattered in a hot plasma surrounding the disk [Compton cloud (CC)]. Specifically, in the low-hard state the energy spectrum of a source is dominated by a power law part, while in high-soft states the thermal disk component is dominant. The Fourier Power Density Spectrum (PDS) also has a specific shape in each state. In low-hard state the source emission is highly variable (up to 40% root-mean-square (rms) variability) and PDS has a broken power law shape with a flat plateau below the break frequency. In a less variable (less than 10 % rms) high-soft state PDS is a power law with index of 1.0-1.5 extending up to an orbital frequency of a binary system (Gilfanov & Arefiev 2006, hereafter GA06) with a cut-off at the higher frequencies. Many efforts have been made to build a consistent theory of PDS formation in accreting sources (see references below). In this Paper we present a model which is based on the exact analytical solution of perturbation diffusion equation in a bounded configuration (i.e. accretion disk or CC). The model explains the continuum shape of the observed PDS components as well as additional effects such as high frequency cut-off and rms-flux relationship (Uttley 2004).

Black hole (BH) and neutron star (NS) sources are characterized by hard and soft states and the transition between them (intermediate states). Vignarca et al. (2003), Kalemci (2003), Titarchuk & Fiorito (2004), hereafter TF04, Titarchuk & Shaposhnikov (2005), hereafter TS05, Shaposhnikov & Titarchuk (2006), hereafter ST06, found that the spectral and timing properties are tightly related to each other in a number of BH and NS sources. Namely, they found observational evidence for the correlation of spectral index with low-frequency features: break frequency ν_b and quasi-periodic oscillation (QPO) low frequency ν_L . In BHs the photon index Γ steadily increases from 1.5 in the low-hard state to values exceeding 2.1 in soft states. In the high/soft state of BH the spectral index-QPO oscillation frequency correlation shows a flattening, or “saturation” of the photon index Γ at high values of the QPO frequency ν_L . This saturation effect was identified as a BH signature. TS05 demonstrate that this saturation is not present at least for one NS source. They show that for 4U 1728-34 the index Γ monotonically increases with ν_L . ST06 found that Cyg X-1 is a perfect example of the BH source where the BH index-QPO frequency correlation is observed with clear features of the saturation at high and low frequencies.

Furthermore, the values of the break frequency and the QPO frequency are related to the BH mass. In principle, one can evaluate the mass of the central object using the index-QPO relation because QPO frequencies are inversely proportional to mass (TF04). The simple scaling of the index-QPO correlation for XTE J1550-564 over the frequency axis gives us the index-QPO correlation for GRS 1915+105. The shifting factor is 10/12 which gives the relative BH mass in XTE J1550-564 with respect to that in GRS 1915+105. However, there is one condition for the method applicability: the index-QPO relations should be self-similar

with respect to each other, as it occurs for GRS 1915+105 and XTE J1550-564.

King et al. (2004) proposed an explicit physical model for the disc variability, consistent with Lyubarskii’s general scheme (Lyubarskii 1997), hereafter L97, for solving this problem. They suggested that local dynamo processes can affect the evolution of the accretion disc by driving angular momentum loss in the form of an outflow (wind or jet). K04 argued that large-scale outflow can only occur when the small-scale random processes in neighboring disk annuli give rise by chance to a coherent large-scale magnetic field. This occurs on much longer time-scales (than that of the small-scale random processes), and causes a bright large-amplitude flare as a wide range of disc radii evolve in a coherent fashion. Most of the time, dynamo action instead produces small-amplitude flickering.

It is worth noting that in our work we offer a method to measure an effective Reynolds number Re using the basic power spectrum parameters (PDS index and characteristic frequencies). We obtain that the inferred Re in the range of 8 ± 2.5 for the Cyg X-1 and Cyg X-2 CC configurations related to their high frequency PDS component (see details §4.2.2). This relatively low value of Re means that there is actually a large turbulent structure (comparable with the size of the accretion flow configuration). Thus we come to the same conclusion that in the bounded disk-like configuration (CC) there is a large turbulent structure which can be a large-scale magnetic field proposed by K04.

K04 also reproduced power spectra similar to those observed, including a $1/\nu$ power spectrum below a break frequency given by the magnetic alignment time-scale at the inner disc edge. Moreover, K04 concluded from in their simulation of power spectra of the accretion disk that the relation between BH mass and the value of the break frequency is less straightforward than often assumed in the literature (cf. ST06). In this paper we demonstrate that the resulting power spectrum of the BH sources is generally a sum of two components: one is presumably related to the innermost part of the disk and another one is related to the oscillations of the extended disk. The values of PDS features (break and QPO frequencies) of the former one are scaled with the BH mass and the break frequency value of the latter component is rather scaled with the disk size and they correlate with the binary orbital frequency (GA06).

Lyubarskii (1997) considered small amplitude local fluctuations in the accretion rate at each radius, caused by small amplitude variations in the viscosity, and then considers the effect of these fluctuations on the accretion rate at the inner disc edge. A linear calculation shows that if the characteristic time-scale of the viscosity variations is everywhere comparable to the viscous (inflow) time-scale, and if the amplitude of the variations is independent of radius, then the power spectrum of luminosity fluctuations is a power-law $1/\nu$. If the amplitude of the variations increases with radius, the slope of the power spectrum of the

luminosity variations is steeper than 1. Lyubarskii pointed out that he had no physical model for the cause of such fluctuations. In particular, although the obvious candidate cause is the magnetic dynamo, the characteristic time-scales for the dynamo are much shorter than the local viscous time-scale. However, K04 modeled the dynamo as a small-scale stochastic phenomenon, operating on roughly the local dynamical time-scale.

L97 and its extension by Kotov, Churazov & Gilfanov (2001) sought also to explain the spectral-timing properties of the X-ray variability of accreting black holes in terms of inward-propagating mass accretion fluctuations produced at a broad range of radii. The fluctuations modulate the X-ray emitting region as they move inwards and can produce temporal-frequency-dependent lags between energy bands, and energy-dependent power PDSs as a result of the different emissivity profiles, which may be expected at different X-ray energies. Kotov et al. (2001) analytically determined spectral-timing properties by making the simplifying assumption that the perturbation introduced into the accretion flow at each radius is a delta function in time and radius.

Recently Mayer & Pringle (2006), hereafter MP06, extended the K04 model by taking proper account of the thermal properties of the disc. Because the degree of variability in the K04 model depends sensitively on the ratio of disc thickness to radius, H/R . MP06 suggested that it was important to follow the time dependence of the local disc structure as the variability proceeds. MP06 agreed that radial heat advection plays an important role in determining the inner disc structure, and also found limit-cycle behavior.

Uttley (2004) and Uttley, McHardy & Vaughan (2005) have pointed out that the existence of a strong linear relationship between the amplitude of the X-ray variability and the X-ray flux - the rms-flux relation - can be used a diagnostic to distinguish between various models. They conclude that simplistic shot noise models that include independent, uncorrelated shots are ruled out by the observed rms-flux relations. On the other hand, Uttley (2004) notes that such a relation can be produced by the model by Lyubarskii (1997).

In this Paper we present the exact treatment of the perturbation diffusion with the generic assumption regarding the disk viscosity, perturbation variability and its distribution in the disk.

We should stress that in our model the emergent signal is a result of the diffusion of the driving (local) perturbations in the disk which is not a composition of independent, uncorrelated shots. In the contrary, in the emergent signal all exponential shots of the composition are related to the spatial distribution of the driving disk perturbations and to the diffusion time scale in the disk. Moreover, the observed rms-flux relation (Uttley 2004) is naturally produced by the perturbation diffusion.

We also demonstrate that the specific shape of the power spectrum is determined by the distribution of the flickering (perturbation) in the configuration, the extended disk or the CC region, and its viscous diffusion time scale t_0 . We study *the effect of the diffusion of these fluctuations on the accretion rate at the inner disk edge*. Wood et al. (2001), hereafter W01, formulated and solved the problem of the diffusive propagation of the initial distribution of the perturbations (Cauchy’s problem) in the disk analytically. We use their general solution to derive the power spectrum of the timing signal which is a response to the diffusion of *the persistent driving* perturbations in the disk-like configuration.

The detailed study of the nature of the driving perturbations of the disk is beyond the scope of the present work. As we mentioned above the local driving perturbations of the disk can be a result of the dynamo as a small-scale stochastic phenomenon, operating on roughly the local dynamical time-scale (see K04). However we suggest that they are likely due to the Rayleigh-Taylor (RT) local instability [e.g. Chandrasekhar (1961) and Titarchuk (2003)] which is a common phenomenon for any configuration with non-homogeneous vertical density structure. These local RT instabilities are usually seen in the Earth atmosphere as gravity waves.

We apply the results of our theoretical investigations to the RXTE and EXOSAT observations of Cyg X-1 and Cyg X-2. Churazov, Gilfanov & Revnivtsev (2001), argued using their data analysis of RXTE observations that the overall shape of the PDS in the soft and hard spectral states can be *qualitatively* explained if the geometrically thin disk is sandwiched by the geometrically thick CC extending in radial direction up to a large distance from the compact object. They also suggested that in the hard state the thin disk is truncated at some distance from the black hole followed by the geometrically thick flow. Our quantitative analysis of PDS and photon spectra of Cyg X-1 and Cyg X-2 confirms this idea. We show that the accretion flow presumably consists of a geometrically thin extended disk component and a geometrically thick CC component.

GA06 analyzed the PDSs for a number of NS and BH sources using RXTE and EXOSAT observations in the wide frequency range, from 10^{-8} Hz to 10^2 Hz. Particularly, they found the composite PDS of Cyg X-2. We reproduce their composite PDS. Furthermore, we infer the physical characteristics of the accretion flow in Cyg X-2 by application of our theory to the observable PDS.

In §2 we present the details of timing signal formation in the source of X-ray radiation. In §3 we detail the main features of the solution of the initial value problem which is tightly related to the shape of the emergent timing signal. We demonstrate these solutions for specific and general cases of disk viscosity as a function of radius. In §4 we show how our theory fits X-ray data from Cyg X-1 and Cyg X-2. Specifically, we explain how the power

spectrum properties correlate with energy spectrum in different spectral states. Discussion of the main results and conclusions follow in §5 and §6.

2. Evolution of the power spectra. Theoretical consideration

In this Paper we study the diffusive propagation of the local dynamical perturbations (fluctuations) in the disk-like bounded configuration. In other words, we assume that there is a temporal source of fluctuation at any point (radius) of the medium (disk) $\Phi(R, t)$. The X-ray time response of the disk, the luminosity perturbation, $\Delta L_x(t)$ can be considered in terms of diffusive propagation of the local driving perturbations $\Phi(R, t)$ in the disk. We assume that the temporal local variation of the mass supply in the disk around the steady state are small. They are only some fraction of the steady state mass supply through the disk. In other words, the amplitude of $\Phi(R, t)$ is proportional to the steady state mass accretion rate. W01 show (see Eq. 7 there) that the mass accretion rate at the innermost radius of the disk $\dot{M}(R_{in}, t)$ is proportional to the mass supply over the disk $A(t)$. It implies that the $\dot{M}(R_{in}, t)$ perturbations, $\Delta \dot{M}(R_{in}, t)$, should be proportional to $\Delta A(t) = 2\pi \int \Phi(R, t) R dR$ and consequently proportional to $A(t)$ because $\Delta A(t) \propto A$.

Thus one can formulate the problem of the diffusive propagation of the surface density perturbations $\Phi(R, t)$ in the bounded configuration (see Eq. 2 and Eq. 5 in W01). It is important to emphasize that this diffusive propagation of fluctuations is an intrinsic property of a given disk-like configuration (necessary condition) where the angular momentum is distributed by diffusion (see Eq. 2).

The resulting power spectrum as a result of the diffusion of perturbations in the disk $\|F_x(\omega)\|^2$ is a product of the power spectrum of the temporal variation of source perturbations $\|F_\varphi(\omega)\|^2$ and the power spectrum of the disk response to the spatial distribution of the driving perturbations over the disk $\|F_Y(\omega)\|^2$ (see Eq. 21). Because the power of the driving perturbations $\|F_\varphi(\omega)\|^2$ is directly related to *the mass supply over the disk* $A(t)$ (see above) the intrinsic property of the diffusive propagation of the driving perturbation is *the existence of a strong relationship between the amplitude of the X-ray variability, related to $\|F_x(\omega)\|^2$, and the X-ray flux $[\propto A(t)]$* [compare with the result of Uttley (2004)].

Thus in the observations we see the dynamical variation in the disk as a variation of the X-ray photon flux. The X-ray spectrum is likely formed as a result of upscattering of the soft Keplerian disk photons in the Compton cloud, which can be regarded as a disk-like sub-Keplerian configuration. One also has to take into account photon diffusion in the power spectrum formation (see Eq. 25). The emergent power spectrum is a result of the combined

effect of the CC photon diffusion and the diffusion of the disk fluctuations i.e. a product of the power spectra for the photon diffusion and fluctuation diffusion respectively (see Eq. 26).

If two disk-like bounded configurations are sources of the perturbation, i.e., $\Delta L_{x,1}(t)$ and $\Delta L_{x,2}(t)$ in the system which are weakly correlated, then the resulting power spectrum is a sum of the corresponding spectra (see Appendix A)

$$||F_x(\omega)|| \approx ||F_{x,1}(\omega)||^2 + ||F_{x,2}(\omega)||^2. \quad (1)$$

2.1. Diffusive propagation of the perturbation in the disk. Formulation of the problem

Here we consider the diffusive propagation when the driving perturbations can be presented in a factorized form $\Phi(t, R) = \varphi(t)f(R)$. In other words a spatial distribution of the driving perturbations in the disk is described by $f(R)$ and $\varphi(t)$ characterizes the perturbation input rate at any disk radius. In Appendix B.1 we show that the diffusion solution for the general case of the function $\Phi(t, R)$ can be well approximated by the solution for $\Phi(t, R) = \varphi(t)f(R)$.

The diffusion equation for the time variable quantity $W(R, t)$, related to the surface density perturbations $\Delta\Sigma(R, t)$, $W(R, t) = \Delta\Sigma(R, t)$, can be written in an operator form (see Eq. 5 in W01):

$$\frac{\partial W}{\partial t} = \mathbf{\Lambda}_R W + \varphi(t)f(R) \quad (2)$$

where R is a radial coordinate in the disk and $\mathbf{\Lambda}_R$ is the space diffusion operator. Equation (2) should be combined with the appropriate boundary conditions at $R = 0$, $R = R_0$ and initial conditions at $t = 0$. For homogeneous initial conditions, namely for $W(R, 0) = 0$ the solution at any R and t can be presented as a convolution

$$W(R, t) = \int_0^t \varphi(t')X(R, t - t')dt'. \quad (3)$$

The kernel of convolution (3), $X(R, t - t')$ is a solution of the initial value problem for the homogeneous equation

$$\frac{\partial X}{\partial t} = \mathbf{\Lambda}_R X \quad (4)$$

with the following initial conditions

$$X(R, t - t')_{t=t'} = X(R, 0) = f(R) \quad (5)$$

and with the same boundary conditions as that for $W(R, t)$ (we specify them in §3, see also Eqs. 15, 16 in W01). The validity of $W(R, t)$, presented by formula (3), as a solution of Eq. (2) with the homogeneous initial condition can be directly checked by its substitution to Eq. (2) having in mind Eqs (4-5) for $X(R, t - t')$.

It is important to point out that resulting perturbation signal is a sum of two components where one component is presented by formula (3) and the other component is a solution of the initial value problem of a homogeneous diffusion equation, analogous to Eqs (4-5) but with the initial perturbation function that can be different from $f(R)$ (see §3).

If the observational time intervals are much longer than the characteristic diffusion time scale of perturbation in the disk t_0 then the contribution of the second component of the resulting signal is exponentially small ¹. The amplitude of perturbations determined by the solution of the homogeneous problem [see Eqs (4-5)] decays exponentially for $t \gg t_0$ (see details in §3).

The power spectrum of $\|F_W(\omega)\|^2$ of $W(R, t)$ can be presented as a product of the power spectra $\|F_\varphi(\omega)\|^2$ and $\|F_X(\omega)\|^2$ of $\varphi(t)$ and $X(R, t)$ respectively:

$$\|F_W(\omega, R)\|^2 = \|F_\varphi(\omega)\|^2 \|F_X(\omega, R)\|^2, \quad (6)$$

where

$$F_W(\omega, R) = \frac{1}{\sqrt{2\pi}} \int_0^\infty e^{-i\omega t} W(t) dt, \quad (7)$$

$$F_\varphi(\omega) = \frac{1}{\sqrt{2\pi}} \int_0^\infty e^{-i\omega t} \varphi(t) dt, \quad (8)$$

$$F_X(\omega, R) = \frac{1}{\sqrt{2\pi}} \int_0^\infty e^{-i\omega t} X(R, t) dt \quad (9)$$

are Fourier transforms of $W(R, t)$, $\varphi(t)$, $X(R, t)$ respectively.

The X-ray resulting variable signal is determined by the fluctuations of the luminosity $\Delta L_x(t)$. We assume that the mass accretion rate variations $\Delta \dot{M}(0, t)$ is converted with efficiency ε_{eff} into the variations of the X-ray luminosity, i.e. $\Delta L_x(t) = \varepsilon_{eff} \Delta \dot{M}(0, t)$.

W01 show that for the function $\mathcal{W}(x, t) = x\hat{\nu}W(x^2, t)$ using a new variable $x = R^{1/2}$ the diffusion equation (2) can be presented in the form

$$\frac{\partial \mathcal{W}}{\partial t} = \frac{3\hat{\nu}(x)}{4x^2} \frac{\partial^2 \mathcal{W}}{\partial x^2} + \varphi(t)\mathcal{F}(x) \quad (10)$$

¹Gilfanov (2006, private communication) points out to the fast decay of this component with time.

where $\hat{\nu}(x)$ is viscosity in the disk, $\mathcal{F}(x) = x\hat{\nu}(x)f(x^2)$. The convolution, similar to Eq. (3), presents the solution $\mathcal{W}(x, t)$

$$\mathcal{W}(x, t) = \int_0^t \varphi(t')\mathcal{X}(x, t - t')dt' \quad (11)$$

where $\mathcal{X}(x, t)$ is a solution of the initial value problem (compare with Eqs. 4, 5)

$$\frac{\partial \mathcal{X}}{\partial t} = \frac{3\hat{\nu}(x)}{4x^2} \frac{\partial^2 \mathcal{X}}{\partial x^2} \quad (12)$$

with the following initial conditions

$$\mathcal{X}(x, 0) = \mathcal{F}(x). \quad (13)$$

W01 (see Eq. 10 there) find that

$$\Delta L_x(t) = \varepsilon_{eff}\Delta \dot{M}(0, t) = 3\pi\varepsilon_{eff}\frac{\partial \mathcal{W}}{\partial x}(0, t). \quad (14)$$

The total X-ray deposition of the fluctuations at the inner disk edge Q_x can be obtained if we integrate Eq. (10) over t (from 0 to ∞) and over x (from 0 to $x_0 = R_0^{1/2}$). Note that the time integral in the left hand side of Eq. (10)

$$\int_0^\infty \frac{\partial \mathcal{W}}{\partial t} dt = \mathcal{W}(x, t)|_{t=\infty} - \mathcal{W}(x, t)|_{t=0} = 0 \quad (15)$$

because we are only interested in the solution for which $\mathcal{W}(x, \infty) = \mathcal{W}(x, 0) = 0$. Thus using the integration of the right hand side of (10) combined with Eq. (14) and the outer boundary condition $\partial \mathcal{W}/\partial x(x_0, t) = 0$ (see W01, Eq. 15) and keeping in mind the relation $x = r^{1/2}$ we find that

$$Q_x = \int_0^\infty \Delta L_x(t)dt = \left[\varepsilon_{eff} \int_0^{R_0} f(R)2\pi R dR \right] \int_0^\infty \varphi(t)dt = C_{dr} \int_0^\infty \varphi(t)dt. \quad (16)$$

Since the function $f(R)$ determines the shape of the spatial distribution of the driving perturbation only, we can normalize $f(R)$ in such a way that the factor C_{dr} in the right hand side of Eq. (16) is equal to 1, namely

$$C_{dr} = \varepsilon_{eff} \int_0^{R_0} f(R)2\pi R dR = 1. \quad (17)$$

In this case the total X-ray fluctuation energy Q_x is equal to the integrated input (flux) of the driving perturbations over the disk:

$$Q_x = \int_0^\infty \varphi(t)dt = Q_{dr}. \quad (18)$$

Eq. (18) implies that the emergent variable flux of X-ray emission Q_x is the same as the integrated input of the driving perturbations over the disk Q_{dr} . In other words *the driving perturbation flux is conserved when the perturbations diffuse through the disk towards the inner disk edge.*

On the other hand *the integrated power of the resulting PDS, P_x is only a small fraction of the integrated power of the driving oscillations, P_{dr} distributed over the disk.* The ratio of P_x/P_{dr} strongly depends on the diffusion timescale in the disk t_0 and on the characteristic frequency of the driving oscillations ν_{dr} , $\nu_{dr} = \omega_{dr}/(2\pi)$.

In fact, the resulting X-ray signal due to the diffusion of the driving perturbations is

$$\Delta L_x(t) = \int_0^t \varphi(t')Y(t-t')dt', \quad (19)$$

$$Y(t) = 3\pi\varepsilon_{eff} \frac{\partial \mathcal{X}(0, t-t')}{\partial x}. \quad (20)$$

To obtain Eqs. (19) and (20) we use Eqs. (11) and (14).

Then the resulting power spectrum is

$$\|F_x(\omega)\|^2 = \|F_\varphi(\omega)\|^2 \|F_Y(\omega)\|^2 \quad (21)$$

where $\|F_x(\omega)\|^2$, $\|F_\varphi(\omega)\|^2$, $\|F_Y(\omega)\|^2$ are Fourier transforms of $\Delta L_x(t)$, $\varphi(t)$, $Y(t)$ respectively [see e.g. Eq. (7) for definition of the Fourier transform]. The disk local driving oscillations convolved with the response of the disk-like configuration results in the emergent response of the system $\Delta L_x(t)$. Ultimately, the power spectrum $\|F_x(\omega)\|^2$ of $\Delta L_x(t)$ carries the information on the characteristic frequencies and the hydrodynamical structure of the system.

In general, the disk driving fluctuation $\varphi(t)$ can be presented as damped quasi-periodic (driving) oscillations for which power spectrum is Lorentzian

$$\|F_\varphi(\omega)\|^2 \propto [(\omega - \omega_{dr})^2 + (\Gamma_{dr}/2)^2]^{-1} \quad (22)$$

where Γ_{dr} is a damping factor. We suggest that the frequency of the disk driving oscillations ω_{dr} (as a frequency of the Rayleigh-Taylor gravity waves) is scaled with the local Keplerian frequency ω_K . In fact, ω_{dr} is some mean value of the rotational frequency of the local quasiperiodic oscillations in the disk-like configuration (see Appendix B.1).

Now we proceed with an estimate of the integrated total power of the resulting signal $P_x = \int_0^\infty \|F_x(\omega)\|^2 d\omega$. Using a relation Eqs (21), (B15), (B18), (B19) we obtain that the integrated total power of the resulting signal

$$P_x = \int_0^\infty \|F_x(\omega)\|^2 d\omega \sim \frac{1}{DQ} \frac{P_{dr}}{\omega_{dr} t_0}. \quad (23)$$

Here $\mathcal{Q} = \omega_{dr}/\Delta\omega \gtrsim 1$ stands for a quality factor, as $\Delta\omega$ stands for a FWHM of $\|F_\varphi(\omega)\|^2$ and a numerical factor $D \gtrsim 1$. We emphasize that $\omega_{dr}t_0 \gg 1$ because the diffusion time scale in the disk t_0 is likely much longer than the timescale of (local) driving oscillation $t_{dr} \sim \omega_{dr}^{-1}$.

Thus using equation (23) we arrive to the conclusion that the *resulting integrated power* P_x , which is related to the perturbation amplitude at the inner disk edge, is much less than the total integrated power of the driving oscillation in the disk P_{dr} ²

$$\frac{P_x}{P_{dr}} \sim (D\mathcal{Q}\omega_{dr}t_0)^{-1} \ll 1. \quad (24)$$

This is a prediction of our diffusion model. The model can be confirmed or refuted if one can determine product of ω_{dr} and t_0 from observations and compare this with the observed ratio of P_x and P_{dr} . In §5 we demonstrate the validity of our model using the power spectrum of Cyg X-1 obtained in the broad frequency range, from 10^{-7} Hz to 10^2 Hz.

Even though the specific mechanism providing the disk viscosity needs to be understood, the diffusion time scale in the disk and driving oscillation frequency “controls” the variability of the innermost region of the accretion disk (Compton cloud). As seen from Eq. (24) the power (rms²) of the resulting disk fluctuations should decrease with ω_{dr} . On the other hand it is well established (see e.g. ST06) that the X-ray emission area (Compton cloud) becomes more compact when the X-ray source evolves from hard to soft states. Average driving oscillation frequency ω_{dr} should progress to higher values during this evolution because it is scaled with some mean ω_K over the Compton cloud. Probably this decrease of P_x/P_{dr} with ω_{dr} is a key to explain the rms decay when the X-ray source evolves from hard to soft states (and when ω_{dr} increases).

2.2. Effect of the photon diffusion in Compton Cloud on the emergent power spectrum

ST06 revealed that the PDS features, break frequency ν_b , and Lorentzian low-frequency ν_L and Q-value of the QPO frequency evolve and increase while the source progresses toward the high-soft state. But the QPO frequencies are completely washed out in the very soft state. Titarchuk et al. (2002), hereafter TCW02, predicted that when the source is embedded in the optically thick medium the QPO features must be absent in the PDS of the source because of photon scattering.

²It should be noted that the referee’s question motivates us to mathematically prove this statement (see Eq. 23).

The strength of QPO frequencies can be easily attenuated when the oscillating X-ray emission passes through the intervening wind environment. The power of the wind presumably related to the mass accretion rate in the disk. In Appendix E we present the details of derivation of the wind outflow rate and optical depth. We also show there that the mass outflow rate is much higher than the mass accretion rate in sources, like Cyg X-1, Cyg X-2 and Sco X-1, with the high supply of the matter from the companion.

Thus we can conclude that the variability of the scattered part of radiation can be completely washed out in the extended wind, of radius of order 10^{11} cm for Cyg X-1, even for the wind optical depth $\tau_W \gtrsim 0.5$ (ST06). The variability of the direct (unscattered) component is preserved but its rms amplitude decreases as $\exp(-\tau_W)$ with τ_W . ST06's data analysis confirms this expectation. The power spectrum in the very soft state is featureless (see ST06, Fig. 6). The emission of the central source is presumably obscured by the optically thick wind and consequently all photons emanating from the central source are scattered. The direct component of the central source radiation that carries information about the variability is suppressed by scattering.

Gies et al. (2003) argue that there is a particular state of Cyg X-1 when the wind velocity is very low, and thus one can expect high accumulation material in the wind and noticeable optical depth of the wind (see also Eq. E15). The wind downscattering of the photons emanating from the inner Compton cloud leads to the softening of spectrum (Titarchuk, & Shrader 2005) and consequently to decrease of X-ray luminosity of the source. The softening of the spectrum can also be a result of effective cooling the Compton cloud by the disk soft photons. If the power law spectra in the soft state are formed in the converging flow, then their indices are determined by the flow temperature (Laurent & Titarchuk 1999, hereafter LT99). The index increases and saturates to the critical value about 2.8 with the mass accretion rate for the low temperatures of the flow (see LT99 and Titarchuk & Zannias 1998).

We can calculate the emergent power spectrum as a result of the diffusive propagation of the perturbations in the disk-like configuration (Keplerian disk or sub-Keplerian Compton Cloud) and the diffusive X-ray photon propagation from the innermost part of the source. The quantitative model of the resulting pulse affected by these perturbations $Z(t)$ can be written as follows:

$$Z(R, t) = \int_0^t \Delta L_x(t') G(t - t') dt' \quad (25)$$

where $\Delta L_x(t)$ is the input pulse of the disk-like source oscillations and $G(t)$ is the photon response pulse of the transition layer (TL). Then the observed power spectrum of $Z(t)$ is a

product of the power spectrum of $\Delta L_x(t)$ (see Eq. 1) and $G(t)$, i.e.

$$\|F_Z(\omega)\|^2 = \|F_x(\omega)\|^2 \|F_G(\omega)\|^2. \quad (26)$$

3. Initial value (Cauchy) problem of diffusion. Diffusion of the radial local perturbations in the disk as an origin of the “white-red” noise. The analytical solution of the problem: General and Particular cases

The diffusive propagation of the perturbation in the disk was studied by W01 in detail. They presented the diffusion equation for the surface density $\Sigma(R, t)$ as a function of time t and the radial position in the disk R (see Eq. 5 in W01). It is worth noting that the derived equation is valid for any disk-like configuration for which the rotational frequency profile is Keplerian. This configuration can be a Shakura-Sunyaev type of disk (Shakura & Sunyaev 1973) or an advection dominated accretion flow (ADAF) (Narayan & Yi 1994, Chakrabarti & Titarchuk 1995). Thus this applies to the Compton cloud as well.

It is also important to emphasize that the equation derived for the surface density can be used as a equation for the surface density perturbations $\Delta\Sigma(R, t)$ in framework of the linear perturbation theory (see also §2.1). In section §2 *we demonstrate that the determination of the diffusion response of the disk to the driving oscillations $\varphi(t)f(R)$ is reduced to the convolution of $\varphi(t)$ with the solution of the initial value (Cauchy) problem for the distributed perturbations at the initial moment $f(R)$* [see Eqs. (4, 5)]. The initial value (Cauchy) problem of the time-dependent diffusive propagation of the surface density perturbation is formulated as follows (see also Eqs. 12, 13):

$$\frac{\partial \mathcal{X}}{\partial t} = \Lambda_{\mathbf{x}} \mathcal{X} = \frac{3\hat{\nu}(x)}{4x^2} \frac{\partial^2 \mathcal{X}}{\partial x^2} \quad (27)$$

with the initial condition

$$\mathcal{X}(x) = \mathcal{F}(x) = x\hat{\nu}(x)f(x^2) \quad \text{at} \quad t = 0 \quad (28)$$

where $x = R^{1/2}$, $\hat{\nu}(x)$ is a viscosity in the disk and

$$\mathcal{X}(x, t) = R^{1/2}\hat{\nu}W = R^{1/2}\hat{\nu}\Delta\Sigma. \quad (29)$$

We combine equation (27) with the boundary condition at the outer boundary

$$\frac{\partial \mathcal{X}}{\partial x} = 0 \quad \text{at} \quad x = x_0 \quad (30)$$

and at the inner boundary $x_{\text{in}} \ll x_0$, $W = \Delta\Sigma = 0$, which is equivalent to

$$\mathcal{X} = 0 \quad \text{at} \quad x = x_{\text{in}}. \quad (31)$$

W01 demonstrated how the mass accretion rate in the disk \dot{M} can be calculated (see Eq.10 in W01). Using the W01's formula and the definition of $\mathcal{X}(x, t)$ in Eq. (29) we can determine of the mass accretion rate perturbation as follows

$$\Delta\dot{M} = 3\pi \frac{\partial\mathcal{X}}{\partial x}. \quad (32)$$

Furthermore, we assume that the perturbation of the mass accretion rate at the inner disk edge is converted with efficiency ε_{eff} into the perturbation of X-ray luminosity, $\Delta_x L(t)$ i.e. $\Delta L(t) = \varepsilon_{\text{eff}} \Delta\dot{M}(t, R_{\text{in}})$ and thus

$$Y(t) \propto \Delta L_x(t) \propto \frac{\partial\mathcal{X}}{\partial x}(t, 0). \quad (33)$$

The solution $\mathcal{X}(x, t)$ of equation (27) with the initial condition (28) at $t = 0$ and boundary conditions (30-31) can be presented using separation of variables as a series

$$\mathcal{X}(x, t) = \sum_{k=1}^{\infty} e^{-\lambda_k^2 t} \frac{\chi_k(x) c_k}{\|\chi_k(x)\|^2}, \quad (34)$$

where $\chi_k(x)$ and λ_k are eigenfunctions and eigenvalues which can be found from the homogeneous ordinary differential equation:

$$\chi_k'' + \lambda_k^2 p(x) \chi_k = 0 \quad (35)$$

combined with the boundary conditions

$$\chi_k = 0 \quad \text{for} \quad x \rightarrow 0, \quad (36)$$

$$\frac{d\chi_k}{dx} = 0 \quad \text{at} \quad x = x_0. \quad (37)$$

$\|\chi_k\|$ is the norm of the eigenfunction, which is calculated through the integral [for example, see the derivation of this formula in Titarchuk, Mastichiadis & Kylafis (1997)]

$$\|\chi_k\|^2 = \int_0^{x_0} p(x) \chi_k^2(x) dx \quad (38)$$

where $p(x) = 4x^2/3\hat{\nu}(x)$ is the weight function and the expansion coefficient

$$c_k = \int_0^{x_0} p(x) \chi_k(x) \mathcal{F}(x) dx. \quad (39)$$

Let us express c_k using eigen-value equation (35)

$$c_k = \int_0^{x_0} p(x)\chi_k(x)\mathcal{F}(x)dx = -\frac{1}{\lambda_k^2} \int_0^{x_0} \chi_k''(x)\mathcal{F}(x)dx. \quad (40)$$

By integration by parts and using boundary conditions (36-37) for $\chi_k(x)$ we obtain

$$c_k = \frac{1}{\lambda_k^2} [\chi_k'(0)\mathcal{F}(0) + \chi_k(x_0)\mathcal{F}'(x_0) - \int_0^{x_0} \chi_k(x)\mathcal{F}''(x)dx]. \quad (41)$$

It is evident from Eq. (41) that

$$c_k \sim \frac{1}{\lambda_k^2} \chi_k'(0)\mathcal{F}(0), \quad (42)$$

for a quasi-uniform initial distribution $\mathcal{F}(x)$, i.e. for which its values and derivatives are bounded. In fact $\chi_k'(0) \propto \lambda_k^\zeta$, where $\zeta > 0$ (see a proof of this below), and $\lambda_k = O(k)$ with increase of k and thus the first term of the right hand side in Eq. (41) is dominant for $k \gg 1$. It is worth noting that formula (42) is exact for $\mathcal{F}(x) = \mathcal{F}(0) = \text{constant}$, namely for the uniform initial distribution of perturbations.

Now we study a case of problems where $\hat{v}(x) = (\hat{v}_0/x_0^\psi)x^\psi$.

3.1. Case with $\psi = 2$

W01 showed that in this case

$$\chi_k(x) = \sin \left[\frac{2}{(3\hat{v}_0/x_0^2)^{1/2}} \lambda_k x \right], \quad (43)$$

and

$$\lambda_k = \frac{(3\hat{v}_0/x_0^2)^{1/2} \pi(2k-1)}{2x_0}. \quad (44)$$

For this particular case the time dependent signal $Y(t)$ is presented as [see Eqs. (33) and (34)]

$$Y(t) \propto \sum_{k=1}^{\infty} [\pi(2k-1)/2] (c_k/|\chi_k|^2) \exp[-\pi^2(2k-1)^2 t/4t_0] \quad (45)$$

where $t_0 = 4x_0^4/3\hat{v}_0 = 4R_0^2/3\hat{v}(R_0)$. t_0 is the viscous timescale and determines both the rise and fall time of the response function $Y(t)$ (see details in W01).

For the uniform perturbation source distribution ($\mathcal{F}(x) = \text{constant}$) (see Eq. 45) we obtain that

$$Y(t) \propto \sum_{k=1}^{\infty} \exp[-\pi^2(2k-1)^2 t/4t_0]. \quad (46)$$

because

$$\|\chi_k\|^2 = \frac{4x_0^2}{3\hat{\nu}_0} \int_0^{x_0} \sin^2 \left[\frac{\pi(2k-1)x}{2x_0} \right] dx = \frac{2x_0^3}{3\hat{\nu}_0} \quad (47)$$

and

$$c_k = \frac{2x_0}{(3\hat{\nu}_0)^{1/2} \lambda_k} \mathcal{F}(0). \quad (48)$$

Using relation (C4) for the power spectrum $\|F_Y(\omega)\|^2$ of $Y(t)$ we obtain that

$$\|F_Y(\nu)\|_\nu^2 \propto \sum_{k=0}^{\infty} \frac{1}{(8t_0\nu/\pi)^2 + (2k+1)^4}. \quad (49)$$

It is worth noting that in Eq. (49) frequencies ν are scaled with the diffusion frequency $1/t_0$. The result of summation in of Eq. (49) can be presented by an exact analytical formula [see Prudnikov, Bruchkov & Marichev (1981), hereafter PBM81, formulas (5.1.28.1)]. Thus

$$\begin{aligned} \|F_Y(\nu)\|_\nu^2 \propto & \frac{\pi}{2^{3/2}a^{3/2}} \frac{\sinh 2^{1/2}\pi a^{1/2} + \sin 2^{1/2}\pi a^{1/2}}{\cosh 2^{1/2}\pi a^{1/2} - \cos 2^{1/2}\pi a^{1/2}} - \\ & - \frac{\pi}{2^{5/2}a^{3/2}} \frac{\sinh \pi a^{1/2}/2^{1/2} + \sin \pi a^{1/2}/2^{1/2}}{\cosh \pi a^{1/2}/2^{1/2} - \cos \pi a^{1/2}/2^{1/2}} \end{aligned} \quad (50)$$

where $a = 8t_0\nu/\pi$. As it follows from this formula that

$$\|F_Y(\nu)\|_\nu^2 = C_N \times \pi^4/96 \quad \text{when } \nu \ll \pi/8t_0 \quad (51)$$

and

$$\|F_Y(\nu)\|_\nu^2 = C_N \times \frac{1}{2^7 \pi^{1/2} t_0^{3/2}} \frac{1}{\nu^{3/2}} \quad \text{when } \nu \gg \pi/8t_0. \quad (52)$$

If the source distribution $\mathcal{F}(x)$ is non-uniform, i.e. $\mathcal{F}(x) \neq \text{constant}$ then in the right hand side of formula (49) an additional term appears (see Eqs. 41-42 for c_k) that is order of $O(1/\nu^2)$ when $\nu \gg \pi/8t_0$. It is a constant for $\nu \ll \pi/8t_0$.

Thus if $|\mathcal{F}(x)|$, $|\mathcal{F}'(x)|$, $|\mathcal{F}''(x)|$ are the same order of magnitude then the sum shown in formula (49) is still the leading term in the corresponding formula for the power spectrum for the non-uniform source distribution. Consequently, the index of the power-law part of $\|F_Y(\nu)\|_\nu^2$ is still equal to 3/2.

3.2. General Case

In this section we investigate the behavior of the power spectrum in the case of arbitrary disk viscosity as a function of R (or $x = \sqrt{R}$). We have already demonstrated for the $\psi = 2$

case that the power spectrum is a constant (the white noise) at very low frequencies ($\nu \ll \pi/8t_0$) and the power law with index $3/2$ at high frequencies $\nu \gg \pi/8t_0$. This shape of the power spectrum is practically independent of the quasi-uniform initial distribution $\mathcal{F}(x)$. We showed that the power spectrum for the $\psi = 2$ case is presented as a series. The calculation of the series is reduced to analytical formula (50) from which low and high-frequency asymptotes are evident (see formulas 51, 52). The similar presentation and asymptotic form of the power spectrum can be obtained in a general case of the disk viscosity.

W01 showed that (see Eq. 38 there)

$$\|\chi_k(x)\|^2 \simeq \mu(x_0)/2. \quad (53)$$

where $\mu(x) = [2/(4 - \psi)](4x_0^\psi/3\hat{\nu}_0)^{1/2}x^{(4-\psi)/2}$. It implies that the normalization of the eigenfunctions $\|\chi_k(x)\|^2$ does not depend on k . On the other hand for small values of the argument x , the eigenfunction χ_k can be presented as,

$$\chi_k(x) = \left[\frac{\pi \lambda_k}{(4 - \psi)} \right]^{1/2} x^{1/2} [\mu(x)\lambda_k/2]^{1/(4-\psi)} / \Gamma[(5 - \psi)/(4 - \psi)]. \quad (54)$$

In fact, it follows from this equation that

$$\chi_k(x) \propto \lambda_k^{(6-\psi)/2(4-\psi)} x \quad (55)$$

when $\lambda_n \mu(x) \ll 1$. Thus

$$[\chi'_k(0)]^2 \propto \lambda_k^{(6-\psi)/(4-\psi)}. \quad (56)$$

The square of $\chi'_k(0)$ is used for calculation of the signal $Y(t)$ (see formulas 33, 34, 41).

Consequently for the uniform perturbation source distribution $\mathcal{F}(x) = \text{constant}$ (see Eq. 42) we obtain that $Y(t)$ can be written as a series (cf. Eq. 45)

$$Y(t) \propto \frac{\partial \mathcal{X}}{\partial x}(0, t) \propto \sum_{k=1}^{\infty} e^{-\lambda_k^2 t} \lambda_k^\delta \quad (57)$$

where

$$\delta = (\psi - 2)/(4 - \psi) \quad (58)$$

($\delta = 0$ for $\psi = 2$) and

$$\lambda_k = \pi[2k - (10 - 3\psi)/2(4 - \psi) - \varepsilon_k/\pi]/2t_0^{1/2}, \quad (59)$$

$$\varepsilon_k = \frac{(2 - \psi)}{(4 - \psi)[(k - 1)\pi + \pi(6 - \psi)/4(4 - \psi)]}. \quad (60)$$

As in the case with $\psi = 2$, t_0 is the viscous time which in the general case is

$$t_0 = \mu^2(x_0) = \frac{4}{3\hat{\nu}(R_0)} \frac{4}{(4 - \psi)^2} R_0^2. \quad (61)$$

One can use equations (59, 60) for calculations of the eigenvalues and ultimately for calculation of the power spectra series (cf. Eq. 49):

$$\|F_Y(\nu)\|_\nu^2 \propto \sum_{k=1}^{\infty} \frac{(2t_0^{1/2} \lambda_k / \pi)^\delta}{(8t_0 \nu / \pi)^2 + (2t_0^{1/2} \lambda_k / \pi)^4} \quad (62)$$

where

$$2t_0^{1/2} \lambda_k / \pi = 2k - (10 - 3\psi)/2(4 - \psi) - \varepsilon_k / \pi \quad (63)$$

which equals $(2k - 1)$ for $\psi = 2$ (see Eq. 49). Although the series of power spectrum

$$\|F_Y(\nu)\|_\nu^2 \propto \sum_{k=1}^{\infty} \frac{[2k - (10 - 3\psi)/2(4 - \psi) - \varepsilon_k / \pi]^\delta}{(8t_0 \nu / \pi)^2 + [2k - (10 - 3\psi)/2(4 - \psi) - \varepsilon_k / \pi]^4} \quad (64)$$

has to be calculated numerically the asymptotic forms of $\|F_Y(\nu)\|_\nu^2$ can be easily evaluated analytically:

$$\|F_Y(\nu)\|_\nu^2 = C_N \times \mathcal{A}_L \quad \text{when } \nu \ll \pi/8t_0 \quad (65)$$

and

$$\|F_Y(\nu)\|_\nu^2 = C_N \times \frac{\mathcal{A}_H}{\nu^{(3-\delta)/2}} \quad \text{when } \nu \gg \pi/8t_0 \quad (66)$$

where

$$\mathcal{A}_L = \sum_{k=1}^{\infty} \frac{1}{[2k - (10 - 3\psi)/2(4 - \psi) - \varepsilon_k / \pi]^{4-\delta}} \quad (67)$$

and

$$\mathcal{A}_H = \frac{1}{2(8t_0 \pi)^{(3-\delta)/2}} \int_0^\infty \frac{x^\delta dx}{1 + x^4}. \quad (68)$$

Similarly to the $\psi = 2$ case the series (64) is the leading term in the general case power spectrum for the non-uniform perturbation source distribution $\mathcal{F}(x)$. For a given ψ the index of the power-law part of the power spectrum (see Eqs. 58, 66)

$$\alpha = (3 - \delta)/2 = (7 - 2\psi)/(4 - \psi). \quad (69)$$

As we have already emphasized in §3.1 that the power spectral density $\|F_Y(\nu)\|_\nu^2$ is a function of dimensionless frequency of νt_0 only (see Eq. 49 and Eqs. 64-68).

In Figure 1 we show the example of white-red noise (WRN) PDS calculated using formula (64) for $\psi = 2$. One can clearly see the low-frequency asymptotic form (white-noise

shoulder) and high-frequency asymptotic form (red-noise power law with index 3/2, see Eqs 65-66) there. For comparison we also show the PDS of an exponential shot which has a Lorentzian shape. For calculation of the WRN PDS we also use analytical formula (50), that is valid when $\psi = 2$, to verify an accuracy of the series summation using formula (64).

3.3. Power spectrum of the signal of the FRED type

If the source of the perturbation is originated in the outer boundary of a given configuration then as shown by W01 the response function $Y(t)$ is characterized by the fast rise and exponential decay function, namely by FRED type burst function (see Eq. 62 in W01):

$$Y(t) \propto (C_0 + C_1/t^{\gamma+1/2}) \exp(-t_0/4t - z_1^2 t/t_0) \quad (70)$$

where

$$C_0 = \sin(\pi\gamma/2 + \pi/4) + (z_1^2)^{\gamma/2} \cos[2(1 - \gamma)/\pi(\gamma - 3)], \quad (71)$$

$$C_1 = 2.5\pi^{-1/2}(t_0/2)^{\gamma+1/2}, \quad (72)$$

$$\gamma = (6 - \psi)/2(4 - \psi), \quad (73)$$

$$z_1^2 = 4u_1/(4 - \psi), \quad (74)$$

and

$$u_1 = (5 - \psi)\{1 - [1 - 2/(5 - \psi)]^{1/2}\}. \quad (75)$$

The power spectrum

$$\|F_Y(\omega)\|^2 = C_N\{C_0^2|I_0|^2 + C_1^2|I_1|^2 + C_0C_1[I_0\bar{I}_1 + I_1\bar{I}_0]\} \quad (76)$$

where

$$|I_j|^2 = I_j\bar{I}_j = (\pi/2)\frac{2^{2(1-\alpha_j)}t_0^{2\alpha_j}}{\rho^{\alpha_j+1/2}} \exp[-2\rho^{1/2} \cos(\varphi/2)], \quad \text{for } j = 0, 1, \quad (77)$$

$$I_0\bar{I}_1 + I_1\bar{I}_0 = (\pi/2)\frac{2^{(3-\alpha_0-\alpha_1)}t_0^{\alpha_0+\alpha_1}}{\rho^{(\alpha_0+\alpha_1)/2+1/2}} \cos[(\alpha_1 - \alpha_0)\varphi/2] \exp[-2\rho^{1/2} \cos(\varphi/2)], \quad (78)$$

$$\rho = (z_1^4 + \omega^2 t_0^2)^{1/2}, \quad (79)$$

$$\varphi = \arcsin(\omega t_0/\rho) \quad (80)$$

and $\alpha_0 = 1$ and $\alpha_1 = 1/2 - \gamma$. The derivation of formula for I_j is presented in the Appendix D (Eq. D2). In Figure 1 we show the example of the FRED PDS. One can see that the FRED PDS exponentially decreases with frequency and this decay is much faster than that for WRN and Lorentzian PDSs.

3.4. The photon (perturbation) diffusive propagation

Any local (photon or hydrodynamical) perturbation in the bounded medium would propagate diffusively outward over time scale (see, Sunyaev & Titarchuk 1980, hereafter ST80 and previous sections for photon and perturbation propagation respectively)

$$t_* \sim f \frac{l_{fp}}{v} \left(\frac{L}{l_{fp}} \right)^2 = f \tau_{pert} \frac{L}{v}, \quad (81)$$

where $L = R_{out} - R_{in}$ is the characteristic thickness of the (photon or hydrodynamical) diffusion configuration, $l_{fp} \sim \eta/(\rho v) = (\sigma_{pert} n)^{-1}$ is the mean free perturbation path, related to the number density n , the interaction cross-section σ_{pert} in the medium, $\tau_{pert} = L/l_{fp} = \sigma_{pert} n L$ and f is a factor which is less than 1 and its exact value determined by the space distribution of photons (perturbations) in the medium (ST80, Sunyaev & Titarchuk 1985, hereafter ST85).

For the diffusive propagation in the bounded medium the response can be also presented as a linear combination of the exponents (see Eq. 34, ST80, ST85)

$$G(t) = \sum_{k=1}^{\infty} A_k e^{-\lambda_k^2 t} \quad (82)$$

where λ_k are the eigen values related to the eigen functions $\chi_k(R)$ of the appropriate space diffusion operator, $A_k = c_k \chi_k(R_{in}) / \|\chi_k\|^2$, $c_k / \|\chi_k\|^2$ is an expansion coefficient of the initial photon (perturbation) function $f(R)$. As we have already shown (see e.g. Eqs. 44-45) $\lambda_k^2 = a_k^2 / t_0$.

For the smooth perturbation source distribution $f(R)$ [all derivatives of $f(R)$ are bounded] and for τ_{pert} of order of one, the response function as a solution of the diffusion problem can be presented by a single exponent (see ST80), namely

$$G(t) \approx A_1 e^{-a_1^2 t / t_0} = A_1 e^{-t / t_*} \quad (83)$$

because $\lambda_1^2 \ll \lambda_k^2$, for $k = 2, 3, \dots$, where $t_* = t_0 / a_1^2$ (for example $a_1^2 = \pi^2 / 4$ for $\psi = 2$).

It is important to emphasize that the response of the diffusive propagation to the initial source distribution of photons (or local hydrodynamical perturbations) $G(t)$ is exactly $A_1 e^{-t / t_*}$ if the source function $f(R)$ is proportional to the first eigenfunction of the space diffusion operator $\chi_k(R)$, i.e. $f(R) \propto \chi_k(R)$.

For this particular response function (see Eqs. 83) the power spectra is Lorentzian

$$\|F_G(\nu)\|_{\nu}^2 \propto [(\nu^2 + (2\pi t_*)^{-2})^{-2}]^{-1}. \quad (84)$$

In Figure 1, we present the Lorentzian PDS along with the WRN and FRED PDSs. It is worth noting that the Lorentzian power-law index is fixed at 2, as for others the PDS power-law index is a function of the viscosity power-law index ψ . One should take into account the effect of photon diffusive propagation in the resulting PDS if the photon diffusion time scale is comparable with the hydrodynamical time scale in the medium. This effect is particularly important for the analysis and interpretation of the high frequency component of the PDS.

Resulting power spectrum

When both perturbation diffusion and photon propagation are taken into account the resulting power spectrum can be presented as a product (see Eq. 26)

$$||F(\omega)||^2 = ||F_x(\omega)||^2 ||F_G(\omega)||^2, \quad (85)$$

where the power spectrum of the hydrodynamical response of the source is a sum of

$$||F_x(\omega)||^2 = ||F_{Y_{in}}(\omega)||^2 ||F_{\varphi_{in}}(\omega)||^2 + ||F_{Y_{out}}(\omega)||^2 ||F_{\varphi_{out}}(\omega)||^2 \quad (86)$$

if the density fluctuations of the inner disk-like component (TL, Compton cloud) are weakly correlated with the fluctuations in the extended Keplerian disk (see Eqs. 1, 21)

4. Applications of the theory to Cyg X-1 and Cyg X-2 data

We now apply the diffusion models to a data sample from the well-studied black hole X-ray binary Cyg X-1. The sample includes observations for all spectral states, from low-hard to high-soft states. An identification number of each RXTE observation of this sample is presented in Table 1. We also show a data sample for Cyg X-2 which is a neutron star (NS) source. Cyg X-2 was always in the high/soft state during RXTE and EXOSAT observations.

4.1. Observations

For our analysis we used Cyg X-1 and Cyg X-2 data from the Proportional Counter Array (PCA) and All-Sky Monitor (ASM) onboard *RXTE* (Swank, 1999) and the medium energy (ME) detector of EXOSAT satellite (Turner, Smith & Zimmermann 1981). The data are available through the GSFC public archive ³. A reader can find the details of Cyg X-1

³<http://heasarc.gsfc.nasa.gov>

observations during the entire *RXTE* era in ST06. These data cover the period 1996 - 2006 (MJD range $\sim 50100 - 53800$).

The ASM instrument operates in the 2 - 12 keV energy range at 3 energy channels and performs flux measurements once per satellite orbit, i.e. every ~ 90 min. Each flux measurement (dwell) has duration of ~ 90 s. Due to navigational constraints and appearance of very bright transient sources, the ASM light curve for particular source sometimes has gaps of duration up to a few months. The dwell-by-dwell light curves at 3 energy channels have been retrieved from the public *RXTE*/ASM archive at HEASARC. EXOSAT provided up to several tens of ks long light curves with a typical time resolution of ~ 1 s in the 0.9–8.9 keV energy range. The EXOSAT data for long-lasting observations have been also retrieved from HEASARC. Their PDSs were computed in the 2 – 12 keV (ASM) and 0.9 – 8.9 keV (EXOSAT ME) energy range. The PDSs of the sources from ASM lightcurves were obtained using the method based on the autocorrelation function calculation described by GA06. The EXOSAT light curves were analyzed with the *powspec* task from *FTOOLS* 5.2. In analyzing the EXOSAT data for that individual PDSs which were similar in shape and normalization, we averaged them to achieve better statistics.

The noise level, calculated for ASM power spectra, although approximately correct, is not accurate enough, due to existence of unaccounted systematic errors in the flux measurements (e.g. Grimm et al. 2002, GA06). This leads to overestimation of values for high frequency part of PDS. This high frequency overestimation can also be related to the specifics of ASM light curves, namely, it can be caused by the aliasing effect leading to the leakage of higher frequency power below the Nyquist frequency. Because for EXOSAT light curves the noise level is not an issue and normalization of EXOSAT PDS spectra are correct we have estimated the ASM noise level using EXOSAT values of PDS for overlapping (for both missions) frequency range. This procedure is reliable for Cyg X-2 data for which PDSs, found from individual EXOSAT sessions, are very similar.

For Cyg X-1 PDSs of individual EXOSAT observation are quite different in shape and amplitude, therefore one should be more careful to smoothly connect ASM and EXOSAT data.

It is known that Cyg X-1 often goes to state transition from regular low/hard state to rarer soft state and vice versa (see ST06 for more details of Cyg X-1 spectral state history). To avoid the influence of such transitions on the composite EXOSAT-ASM power spectrum we have separately calculated PDS for low/hard and soft states of Cyg X-1. To identify a spectral state we have calculated the power-law index of the photon spectrum Γ based on ASM data from different energy channels (Smith et al. 2002). For low/hard state we have collected individual dwell measurements with $\Gamma < 1.5$. For soft state we have chosen

observations with $\Gamma > 2.5$ from 2002 year only. This period was uniquely long when Cyg X-1 stayed most of the time in the soft state.

We also employ a similar procedure to find the appropriate high-frequency (PCA) part of a broadband PDS. Namely, we identify a group of PCA observations by photon spectral index, i.e. observations in a similar spectral state and choose the one with PDS low-frequency part most closely matching the appropriate high-frequency part of EXOSAT PDS where they overlap. Both RXTE/PCA photon spectra and PDS were corrected for an effect caused by detector dead time after each event detection. Deadtime in energy spectra was based on “The RXTE Cookbook”⁴ recipe. The details of PDS deadtime correction are described in Revnivtsev, Gilfanov & Churazov (2000).

4.2. Results of Data analysis and Their Interpretation

4.2.1. Power spectrum evolution vs. photon spectrum evolution

Our theoretical model reproduces the observable PDS shape of Cyg X-1 down to low frequencies (see Fig. 2 - 3). Note all observational PDSs are presented in units of rms^2/Hz throughout the paper. In the low-hard and high-soft states the power spectrum continuum is fitted by our diffusion model. However, one or two relatively broad Lorentzians are needed for fitting of QPO features observed in the low-hard and intermediate states of Cyg X-1.

We clearly see two independent hydrodynamical components in the accretion flow. Their presence are confirmed by power and photon spectra. They are presumably related to an extended Keplerian disk (Shakura & Sunyaev 1973) and a compact geometrically thick sub-Keplerian halo-Compton cloud (see Chakrabarti & Titarchuk 1995, Narayan & Yi 1994). In Figures 2 and 3 we present the observable evolution of RXTE/PCA PDS and photon spectra of Cyg X-1. PDS is fitted by a product of a sum of LF and HF WRN power spectra and a zero-centered Lorentzian (see Eqs. 21, 22, 85-86) plus the narrow Lorentzians to fit QPO features. This model is consistent with the data. In fact, we do not see any difference in the fits of the observed PDSs if we use either a zero-centered Lorentzian or the driving oscillation Lorentzian of frequency ν_{dr} with quality factor $Q \gtrsim 1$.

A black line is for the resulting PDS as red and blue lines present the LF component $||F_{Y_{in}}(\omega)||^2 ||F_G(\omega)||^2$ and HF components $||F_{Y_{out}}(\omega)||^2 ||F_G(\omega)||^2$ respectively. It is evident that from our fitting procedure (see Eq. 85) that the photon diffusion time as the best-fit

⁴<http://heasarc.gsfc.nasa.gov/docs/xte/data.analysis.html>

parameter t_* of $\|F_G(\omega)\|^2$ is the same for the LF and HF components of the spectra (see red and blue lines in left panels of Figs. 2 and 3). We cannot separate them out for each of these individual components. It is worth noting that the model is valid if the variability time scales of the driving oscillations $\varphi_{in}(t)$ and $\varphi_{out}(t)$ are much shorter than the relating diffusion time scales of the CC $t_{0,in}$ and extended disk $t_{0,out}$ respectively. The values of the model best-fit parameters for an observational sample are given in Table 1.

We use ASM and EXOSAT data in order to extend the PCA PDSs presented in Figs. 2-3 to much lower frequencies. In Figure 4 we show two composite EXOSAT/PCA PDSs of Cyg X-1 for the low/hard state. For presentation purposes the upper PDSs is multiplied by additional factors of 10^3 . Note, the data sets of EXOSAT/ME and RXTE/PCA PDSs were collected at different times and thus to make the composite EXOSAT/ME and RXTE/PCA PDSs we constructed them by matching low-frequency part of PCA PDS with high-frequency part of EXOSAT PDS.

We have plotted EXOSAT power spectrum of 24 July 1984, observation with the best timing resolution available 0.2 s, in Figure 5. We have also fitted EXOSAT data by our LF-HF diffusion model. No photon diffusion effects were taken into account for this fit as for typical values of photon diffusion time t_* are of the order of 1 ms (see Figure 7) for which PDS shape for less than 10 Hz is not affected (see discussion below). One can see that this particular EXOSAT PDS is well described by our LF-HF diffusion model ($\chi^2 = 1.27$). It is worth noting that *the low frequency power-law slope is either barely observed or not observed at all in PCA data alone at low/hard state from 0.01 Hz to 100 Hz (Figs. 2, 3) but it can be clearly seen at longer time scales, probed with EXOSAT.*

Thus, EXOSAT observes the presence of low frequency power slope related to LF part of our model along with the presence of high frequency power slope which is the HF part of our model. One can expect that low frequency and high frequency power-law slopes can always be observed in the power spectrum of low/hard state of Cyg X-1 if one could have simultaneously long observations with high timing resolution.

ASM/PCA PDS of the high-soft state is shown on Figure 6. All PDSs shown in Figures 4 - 6 are well fitted by our LF-HF component model, a reader can find values of the best-fit parameters and χ^2 for these particular PDSs in the figure captions. The success of the fitting the data with this additive LF-HF PDS diffusion model (see Eqs. 1, 86) provides *a strong evidence for the presence of two weakly correlated components in accretion flow of Cyg X-1.*

It is worth noting that the photon diffusion PDS, $\|F_G(\omega)\|^2$ makes a difference in the high frequency part of PDS only. The photon diffusion PDS is flat for frequencies $\nu \ll 1/(2\pi t_*)$ (see Eq. 84). In fact, the photon diffusion time scale t_* is obtained using a high-frequency

turnover in PDS (see Figs. 2-3) and t_* is related to the photon-crossing time scale of the CC-wind (photon diffusion) configuration, $t_{cross} = L/c$, namely

$$t_* \sim f\tau_0 L/c = f\tau_0 t_{cross} \quad (87)$$

where $\tau_0 = \tau_{CC} + \tau_W$ is a sum of Thomson electron optical depths of Compton cloud τ_{CC} and wind τ_W (see also Eqs. 81, E15).

In Figure 7 we show how the best-fit parameter t_* depends on Γ . For $\Gamma > 1.9$ (for intermediate and soft states) the photon diffusion time t_* correlates with Γ . t_* reaches the highest value about 20 ms in the soft state. In this state the optical depth of $\tau_0 = \tau_{cor} + \tau_W \gtrsim 3$ (see ST06) and thus using formula (87) we find that the photon diffusion size $L \sim ct_*/(f\tau_0)$ is more than 2×10^8 cm. The distribution of t_* vs Γ is flat for states for which $\Gamma < 1.9$ with some indication of anticorrelation of t_* vs Γ . The values of t_* are about 1 ms. This anticorrelation is presumably related to the contraction of the Compton cloud when the source only starts progressing towards the soft state and the strong wind is not formed yet (see ST06). The hard-to-soft spectral transition in Cyg X-1 is likely caused by an increase of the mass accretion rate in the extended disk. On the other hand, when the mass accretion rate increases the strong wind is launched (see Proga 2005 and Appendix E) that leads to the rise in the optical depth of the wind τ_W and eventually to the correlation of t_* with Γ (see Eq. 87). We also see the manifestation of the strong wind development during the spectral transition as an appearance of the strong iron K_α line and disappearance of the QPO features in the power spectrum that are washed out in the wind (see ST06 and §2 for more details).

Photon spectrum is fitted by BMC+GAUSSIAN model. In Figures 2-3 (right hand panels) the resulting spectrum is shown by black curve while the BMC blackbody and Comptonization components are shown by red and blue lines respectively. The gray line presents the Gaussian shape of K_α line located at 6.4 keV. The power of the LF white-red noise component increases with the increase of the power of the BMC BB component and strength of K_α line (compare Figures 2 and 3). The HF white-red noise component is shifted to the higher frequencies than that in the hard state presented in Fig. 2. In the soft state (see Fig. 3, bottom panel) the LF white-red noise component (red line) dominates the PDS and the intensity of the BMC BB component reaches the highest value.

Comparison of the our PDS model with the data shows that the perturbation (fluctuation) distribution in the accretion flow is rather smooth. The concentrated fluctuations at the outer edge, δ -function type of fluctuation and their diffusive propagation throughout the disk as an origin of the variable time signal (light curve) is ruled out by the observations. The fluctuations are well distributed over the accretion configuration. The time scale of the driving fluctuation in the flow is much shorter than the disk diffusion time scale. This

statement is true for all spectral states. Probably, the steepness of PDS at high frequencies that occurs in all spectral states can be a sign of high frequency fluctuations in the accretion flow. More precise estimate of the time scale of the driving oscillation requires further investigation.

It is important to emphasize that the index of the WRN PDS changes depending on the spectral state. It is not fixed at the value about one (cf. L97). In fact, the real value of the index (see Eq. 69) provides us information regarding the viscosity distribution in the accretion flow and ultimately about hydrodynamical characteristics of the accretion flow, namely Reynolds number Re .

4.2.2. Reynolds number of the flow and Shakura-Sunyaev disk α_{SS} - parameter as observable quantities

Using the best-fit parameters of the PDS model we can infer the evolution of the physical parameters of the source such as the disk diffusion time t_0 , magneto-acoustic QPO frequency ν_{MA} and Reynolds number of the accretion flow Re , with the change of photon index. We can relate t_0 with Re and ν_{MA} (see Eq. 61)

$$t_0 = \frac{4}{3} \frac{4}{(4 - \psi)^2} \left[\frac{V_{MA} R_0}{\hat{\nu}(R_0)} \right] \left(\frac{R_0}{V_{MA}} \right) = \frac{4}{3} \frac{4}{(4 - \psi)^2} \frac{Re}{a_{MA} \nu_{MA}}. \quad (88)$$

where a_{MA} is a numerical coefficient. To relate V_{MA}/R_0 ratio with ν_{MA} we use a formula for magneto-acoustic oscillation frequency derived by Titarchuk, Bradshaw & Wood (2001), hereafter TBW01 (see Eqs. 13, 16 and 17 there):

$$\nu_{MA} = V_{MA}/(a_{MA} R_0) \quad (89)$$

where $a_{AM} \sim 2\pi$ is for a pure acoustic case without magnetic field ($\alpha = 0$ in Eqs. 13, 17 in TBW01) and $a_{AM} \sim 1$ is for a pure magnetic case ($\alpha = 6$ see Eqs. 13, 16 in TBW01). The values of a_{AM} presented here are for the free boundary conditions (see TBW01 for details) which are presumably appropriate for the disk-like configurations around BHs. Formula (88) leads to equation

$$Re = a_{AM} \frac{3}{4} \frac{(4 - \psi)^2}{4} (\nu_L t_0) \quad (90)$$

that allows us to infer a value of Re using the best-fit model parameters t_0 and the QPO low frequency ν_L presumably equals to ν_{MA} . Ultimately we can find the evolution of Re with the photon index Γ because the viscosity index ψ and the product $\nu_L t_0$ evolves with Γ (see Figs. 8, 9, Table 1).

In Figure 8 for the HF white-red noise component we present the best-fit diffusion frequency (which is inverse of the best-fit diffusion time scale t_0) vs photon index Γ (upper left panel), QPO low frequency ν_L vs Γ (right upper panel), the best-fit index of the radial viscosity distribution, ψ vs Γ (lower left panel) and the inferred Reynolds number Re , using t_0 , ν_L , ψ , and Eq. (90), vs Γ (lower right panel). One can clearly see that the CC shrinks when the source moves towards the soft state: QPO frequency ν_L and inverse of the diffusion scale t_0^{-1} increase when the source evolves to higher indices. Also the viscosity $\hat{\nu} \propto R^{\psi/2}$ tends to concentrate to the innermost part of the flow: the viscosity index ψ decreases with the photon index. Despite these correlations of the flow parameters the Reynolds number Re does not vary much within error bars shown in Fig 8, namely $Re \sim 8 \pm 2.5$ (or $\alpha = 1/Re \sim 0.14 \pm 0.04$).

4.2.3. Diffusion time and QPO frequency

One can see that our model describes the dynamical behavior of power spectra with physically meaningful parameters. Indeed, according to the theory (Eq. 61), viscous time is proportional to R_0^2 , square of configuration size (or diffusion frequency $1/t_0 \propto 1/R_0^2$) while QPO frequency is proportional to $1/R_0$. As it was already mentioned (see also ST06) the change in the power index of energy spectra follows the change in the size of emitting region (CC-wind configuration). One can see from Figure 8 that the QPO frequency changes by one order of magnitude as the diffusion frequency $1/t_0$ (as the best-fit parameter of observed PDS) changes by two orders of magnitude. This changes correspond to the change in the power-law index of photon spectra from 1.5 to 2.0 and therefore to the change in size of emitting region.

Another way to demonstrate that Compton cloud contracts when the source evolves to the softer states is to present a product $\nu_L t_0$ as a function of Γ (see Fig. 9). $\nu_L t_0$ according to our model is a monotonic function of R_0 (see Eqs. 88-89). Thus one can conclude using the inferred dependence of $\nu_L t_0$ vs Γ that Compton cloud size R_0 really decreases when Γ increases (i.e. when source moves to the softer states). This behavior of observed QPO and diffusion (time) frequencies is naturally expected in the framework of the our diffusion model. It proves that our model gives predictive and physically meaningful estimates of dynamical behavior of the diffusion medium.

4.2.4. Power-law viscosity index

We also found that the power-law viscosity index ψ of the LF frequency component of PDS depends on the photon index Γ (see Fig. 10). It increases with Γ and then saturates to $\psi = 2.9 \pm 0.1$ for $\Gamma > 2.3$. If we assume that the product $\nu_L t_0$ is of the order of one through all states for the LF frequency component of PDS then we obtain that $\text{Re}_{\text{LF}} \sim 1.5$. In other words the extended disk related to the LF frequency component of PDS (LF WRN) could have higher viscosity than that in the CC flow. In fact, $\hat{\nu} \propto 1/\text{Re}$ (see Eq. 88) but the CC Re_{HF} (~ 8) is less than the extended disk Re_{LF} (~ 1.5).

4.2.5. The composite power spectrum of Cyg X-2

We also constructed the composite PDS for a neutron star source Cyg X-2 using ASM-PCA of RXTE and EXOSAT data on Figure 11. Cyg X-2 is most of the time in high-soft state, when the photon spectral index is about 4 and higher. We found that the broadband PDS in Cyg X-2 has the structure similar to Cyg X-1. Namely, PDS consists of two (LF and HF) components. We fit Cyg X-2 PDS using our two components model. For the LF PDS component the best-fit parameters are: $t_{D,0} = (6.7 \pm 1) \times 10^5$ s, $\psi_D = 1.66 \pm 0.06$, and for the HF PDS component they are $t_{C,0} = 0.8056 \pm 0.0001$ s, $\psi_{CC} = 3.11 \pm 0.02$. QPO lowest frequency is $\nu_L = 60.03 \pm 2.25$ Hz.

TBW01 demonstrated that the magneto-acoustic QPO frequency for a number of NS sources is mostly determined by the magnetic (Alfven) frequency ν_M . Thus in order to calculate the Reynolds number of the CC flow Re_{CC} in Cyg X-2 (NS) we should apply formula (90) in which the numerical factor $a_{AM} \sim 1$ (a pure magnetic case). Using the values of the best-fit parameters of the HF component (see above) related to the CC configuration we obtain that $\text{Re}_{CC} \sim 7.5$ (or the corresponding $\alpha_{\text{SS}} \sim 0.14$). It is interesting that for Cyg X-2 the inferred values of Re_{CC} and $\alpha_{\text{SS},CC}$ are very close to that found in Cyg X-1 (BH).

5. Discussion

The main goal of the presented work is to demonstrate that the emergent timing variability of X-ray emission from compact sources is a result of the diffusive propagation of the driving perturbations which are distributed over the disk. This effect is an intrinsic property of any bounded disk-like configuration. We solved a problem of the diffusive propagation of the driving perturbations (fluctuations). We demonstrate that the solution of this problem is reduced to the solution of the initial value problem with distributed sources at the initial

moment. The formulation is general and classical. The local driving fluctuations, possibly Rayleigh-Taylor local instabilities, gravity waves or the dynamo as a small-scale stochastic phenomenon, operating on roughly the local dynamical time-scale, are high-frequency damped quasi-periodic oscillations which frequencies are related to the local Keplerian frequencies. The driving oscillation amplitude is assumed to be a smooth function of the radius.

The basis of the presented power spectrum formation scenario is that the timing signal is a result of diffusive propagation of driving perturbations in the bounded configuration (disk or Compton cloud) in the same way as X-ray photon spectrum is a result of the photon diffusion (namely, upscattering of seed photons) in the same bounded configuration. The problem of the diffusive propagation of the space distribution of high-frequency perturbations is formulated as a problem in terms of the diffusion equation for the surface density perturbations. This equation is combined with the appropriate boundary conditions (see sections 2, 3).

Our solution is a convolution of the solution of the initial value problem and the source distribution function (see §2.1 and §3). The solution of the initial value (Cauchy) problem is a linear superposition of exponential shots which are *not independent*. For example, if the driving perturbations are distributed according to the first eigen-function of the diffusion operator (see §3.4) then the bounded medium works as a filter producing just one exponential shot as a result of the diffusive propagation of eigen-function distribution of the seed perturbations. In the general case the resulting signal is a linear superposition of exponential shots which are *related* to the appropriate eigen-functions. Furthermore, in section 2 we demonstrate that *the observed rms-flux relations* (e.g. Uttley, McHardy & Vaughan 2005) is naturally explained by the diffusion solution (model). In the framework of the linear diffusion theory the emergent perturbations are always linearly related to the driving source perturbations through a convolution of the Green function and source distribution (see Appendix B and §2.1).

The asymptotic form of the power spectrum [Eqs. (65), (66)] is characterized by a flat shoulder (white noise) when the frequency is less than the inverse diffusion timescale in the disk. In other words the LF WN shoulder is insensitive to the viscosity law in the disk as a function of radius. The second HF asymptotic form is a power law with an index which is sensitive to the viscosity and perturbation source distribution in the disk. When the viscosity *linearly* increases with radius and the perturbation sources $f(r)$ are quasi-uniform then the index α is exactly $3/2$ (see formulas 50 and 52). When the disk viscosity is proportional to $R^{\psi/2}$, the PDS power-law index is $\alpha = (3 - \delta)/2$, where $\delta = (\psi - 2)/(4 - \psi)$ ($\delta = 0$ for $\psi = 2$). We thus establish that the extended power law “red noise” $1/\nu^{(3-\delta)/2}$ is a signature of diffusive propagation of smoothly distributed perturbations in the extended

bounded medium (in our case, a disk-like configuration, e.g. Keplerian disk or ADAF type configuration). In other words WRN is a generic consequence of the diffusion theory rather than a specific property of some particular model for the variability in accretion disks. It is worth noting this WRN shape of the PDS continuum is seen for frequencies which are less than the characteristic frequency of the driving oscillations. We found that the WRN model is consistent with the observations up to high frequency cutoff in the PDS, which may be an indication of high frequency variability of the driving perturbations in the disk. The steepness of PDS at high frequencies that occurs in all spectral states may also be a sign of high frequency fluctuations in the accretion flow and photon diffusion in the CC-wind configuration.

In Figure 12 we present two particular examples of PDS (left panels) of two BHC GRO J1655-40 and XTE 1859+226 where the driving QPOs ν_{dr} are presumably detected by RXTE/PCA. One can clearly see signatures of ν_{dr} at $\sim 10 - 20$ Hz for GRO J1655-40 (top) and ~ 185 Hz for XTE 1859+226 (bottom) before a high-frequency cut-off. The continuum of GRO J1655-40's PDS is well fitted by the white-red noise (WRN) model. The WRN shape is seen at all frequencies which are less than of ν_{dr} . The PDS continuum of XTE 1859+226 is fitted by a sum of LF WRN and HF WRN. There is a strong QPO low frequency ν_L at ~ 7.5 Hz near a break frequency of HF WRN.

One can put a fair question how the rms² power of the driving (source) quasi-periodic oscillations is related to the observed rms² (resulting) power which is a result of the diffusive propagation of the driving perturbations in the disk. In §2.1 (see Eq. 24) we argue that the resulting power of the emergent signal is much less than the power of the source (driving) perturbations.

The simplest way to estimate a contribution of the perturbation at a given frequency to the total rms² power is to construct a power $\times\nu$ diagram. In Figure 12 we present PDS $\times\nu$ diagrams of GRO J1655-40 and XTE 1859+226 (right top and bottom panels respectively). The rms² power at ν_{dr} of order of 10^{-3} rms² is comparable to (GRO J1655-40) or higher (XTE 1859+226) than that at lower frequencies (see right panels). The total rms² power can be estimated as a sum of power $\times\nu$ over all decades of frequencies. Because the diffusion (break) frequencies of LF components of GRO J1655-40 and XTE 1859+226 presumably occur at frequencies much less than 10^{-2} Hz (they are not visible in the presented PDSs) we can only guess that the total power is presumably of order of 10^{-2} rms².

On the other hand in the composite ASM/PCA power spectrum of Cyg X-1 (see Fig. 6) the break frequency of LF component is clearly identified at about 10^{-6} Hz. It should be noted that the RN high-frequency tail has a cutoff around 10 Hz which can be an indication of the driving perturbation frequency, i.e. $\nu_{dr} \sim 10$ Hz. Thus we can cal-

culate the total rms² power by a direct integration of the power spectrum. In order to calculate this power one should integrate the red noise (RN) component of the resulting PDS $\|F_x(\nu)\|_{\nu,RN}^2 \sim 10^4(\nu/10^{-6} \text{ Hz})^{-1.06}\text{rms}^2/\text{Hz}$ and the white noise (WN) component $\|F_x(\nu)\|_{\nu,WN}^2 \sim 10^4 \text{ rms}^2/\text{Hz}$. It is obvious that the RN component power $P_{RN} = 0.44 \text{ rms}^2$. The integration of the WN PDS component from 0 to 10^{-6} Hz gives us that the WN component power $P_{WN} = 10^{-2}\text{rms}^2$. Thus the total power $P_{tot} = P_{RN} + P_{WN} \approx 0.45 \text{ rms}^2$. It is easy to check that the similar estimate can be obtained using multiplication of this PDS by a frequency ν followed by summation of a power $\times\nu$ over frequency decades.

We remind a reader that the resulting power spectrum is a product of WRN and driving oscillation power spectra (see formulas 21 and B10). An interesting question is what is a relative contribution of the WRN PDS and the driving oscillation PDS in the resulting PDS of Cyg X-1.

In fact, the WRN PDS is normalized to $1/(Dt_0)$ where $D \gtrsim 1$ (see Eqs. B16). The diffusion time scale in the disk t_0 as the best-fit parameter of WRN PDS in Cyg X-1 equals to 6×10^5 s (see Fig. 6). Thus in this case of Cyg X-1 the WRN PDS should be presented as followed

$$\|F_Y(\nu)\|_{\nu}^2 \approx A_N \begin{cases} 1 & \text{if } \nu \leq 10^{-6} \text{ Hz} \\ (\nu/10^{-6}\text{Hz})^{-1.06} & \text{if } \nu \geq 10^{-6} \text{ Hz} \end{cases} \quad (91)$$

where $A_N \approx 0.1$ is a normalization constant.

Using the total power of the driving oscillations P_{dr} we can rewrite the driving oscillation PDS as (see Eqs. 22 and B5)

$$\|F_{\varphi}(\nu)\|_{\nu}^2 = \frac{\hat{\Gamma}_{dr}P_{dr}/(a\pi)}{(\nu - \nu_{dr})^2 + (\hat{\Gamma}_{dr}/2)^2} \quad (92)$$

where $\hat{\Gamma}_{dr}$ is a full width of half maximum (FWHM) of the Lorentzian and a constant a varies in the range between 1 and 2 depending on the ratio of $2\nu_{dr}/\hat{\Gamma}_{dr}$ (for example $a = 1$ and $a = 2$ when $2\nu_{dr}/\hat{\Gamma}_{dr} \ll 1$ and $2\nu_{dr}/\hat{\Gamma}_{dr} \gg 1$ respectively). At frequencies $\nu \ll \nu_{dr}$ the driving PDS is a constant

$$\|F_{\varphi}(0)\|_{\nu}^2 = \|F_{\varphi}(0)\|_{\nu}^2 = \frac{\hat{\Gamma}_{dr}P_{dr}/(a\pi)}{\nu_{dr}^2 + (\hat{\Gamma}_{dr}/2)^2}. \quad (93)$$

Because for any power spectrum $\|F(\omega)\|^2$

$$\|F(\omega)\|^2 d\omega = \|F(2\pi\nu)\|^2 2\pi d\nu = \|F(\nu)\|_{\nu}^2 d\nu$$

we have that (compare with Eq. 21)

$$\|F_x(\nu)\|_{\nu}^2 = (2\pi)^{-1} \|F_{\varphi}(\nu)\|_{\nu}^2 \|F_Y(\nu)\|_{\nu}^2. \quad (94)$$

From Eqs. (91), (93), (94) we obtain that for the ASM/PCA power spectrum of Cyg X-1

$$\|F_\varphi(0)\|_\nu^2 = 2\pi\|F_x(0)\|^2/\|F_Y(0)\|^2 = 2\pi \times 10^4/0.1 \text{ (rms}^2/\text{Hz)} \sim 6 \times 10^5 \text{ (rms}^2/\text{Hz)}. \quad (95)$$

As an application of the preceding analysis we can conclude that $P_{dr} \gtrsim 6.3 \times 10^6 \text{ rms}^2$ because $P_{dr} \gtrsim \nu_{dr}\|F_\varphi(0)\|_\nu^2$. If we compare this with the integrated power $P_x = P_{tot} = 0.45$ for the Cyg X-1 PDS (see Fig. 6) we find that the integrated power of the driving oscillations P_{dr} is higher by 7 orders of magnitude than that for the emergent signal, namely $(P_{dr}/P_x)_{CygX-1} \gtrsim 1.4 \times 10^7$. In other words *the resulting observed integrated power is very small fraction ($\sim 10^{-7}$) of the integrated power of the entire disk*⁵. This is precisely what was predicted by our analysis of the diffusion model (see Eq. 24). In fact, the theoretically predicted ratio

$$\left(\frac{P_x}{P_{dr}}\right)_{diff} \sim \frac{1}{2\pi\nu_{dr}t_0\mathcal{QD}} = \frac{1}{(2\pi \times 10\text{Hz})(6 \times 10^5\text{s})\mathcal{QD}} = 2.6 \times 10^{-7}/(\mathcal{QD}) \quad (96)$$

is comparable with that inferred for the observed Cyg X-1 PDS. Namely

$$\frac{(P_x/P_{dr})_{CygX-1}}{(P_x/P_{dr})_{diff}} \sim 0.5\mathcal{QD} \sim 1 \quad (97)$$

where a factor $\mathcal{QD} \gtrsim 1$.

We emphasize that the presented theory (model) provides new physical insights into accretion processes that occur around compact objects:

1. We shed light on the nature of the power spectrum continuum. The PDS shape is a white-red noise which is a result of diffusive propagation of high-frequency damped quasi-periodic driving oscillations. The shape is determined by the disk diffusion time scale and the viscosity distribution in the disk.
2. The ‘‘rms-flux relation’’ found in the observation [see e.g. Uttley (2004) and Uttley et al. 2005] is naturally explained in the framework of the diffusive propagation of the disk perturbations.
3. The decay of the variability power within 0.1-10 Hz frequency range during the source evolution from the hard to soft states is well known observational phenomenon. We found that this effect is a natural consequence of the diffusive propagation of high-frequency driving oscillations. We demonstrate, using the diffusion theory and observed Cyg X-1 PDS, that the integrated power of the resulting PDS P_x is only a tiny

⁵The referee was first who inferred this ratio using the Cyg X-1 PDS presented in Fig. 6.

fraction of the integrated power of the driving oscillations P_{dr} distributed over the disk. Furthermore, we demonstrate that the resulting power P_x is inversely proportional to the characteristic frequency of the driving oscillations ν_{dr} , which is presumably scaled with the frequency of the local gravity waves in the disk (Keplerian frequency). When the source evolves to softer state, the Compton cloud region becomes more compact (see ST06) and thus the power P_x declines towards soft states.

4. To fit the observed PDSs we use WRN model for the continuum and Lorentzians to determine the various QPO frequencies seen as bumps in PDS. As a result of this fitting, in particular, we found the diffusion time of Compton cloud disk-like configuration t_0 and the low QPO frequency (see Fig. 8 in the paper) is a function of photon index. It is seen from Fig. 8 that as QPO frequency changes by one order the inverse of t_0 (a diffusion frequency) changes by almost two orders of magnitude in a given photon index range. This is a real self-consistency check of the diffusion theory vs observations because QPO frequency ν_L is proportional to $1/R_0$ and $1/t_0$ is proportional to $(1/R_0)^2$ (R_0 is the Compton cloud size).
5. The rising QPO frequency and decreasing $t_{C,0}$ with the spectral index Γ is a signature of the Compton cloud contraction as it progresses towards the soft state. QPO frequencies varies inversely with the size of the region. (see ST06 for details of spectral and timing analysis of X-ray data for Cyg X-1 collected with the *RXTE*).
6. The best-fit model parameters ν_L and t_0 allow us to determine Reynolds numbers Re directly from the observed power spectra. Thus, our model provide an opportunity to study the magnetohydrodynamics of the accretion flow directly by using the observed PDS. We found that Re has a constant physical value (within the error bar range) as a function of several varying parameters (diffusion time, QPO frequency and the WRN power-law index).

6. The main results and conclusions

We conclude by summarizing the main results of the presented diffusion theory.

We have presented a detailed mathematical analysis of the perturbation diffusive propagation. We investigated the intrinsic properties of the disk density evolution equation (27) with the appropriate boundary and initial conditions in a general case. We have analyzed the diffusion models determined by the disk viscosity dependence on the radius for various perturbation sources in the disk. We have examined the case where the viscosity is a power law function of position in the disk. Using the perturbations of the disk surface density $\Delta\Sigma(r, t)$

we are able to infer the evolution of the perturbations of the mass accretion rate in the inner disk edge and ultimately the perturbations of the X-ray luminosity as a function of time, $\Delta L_x(t)$. Then we calculate the power spectrum using the Fourier transforms of $\Delta L_x(t)$ and the driving perturbations. The PDS continuum (White-Red-Noise) is a power spectrum of the diffusion response of the disk-like configuration to the high frequency (local) driving disk oscillations. Whereas X-ray photon spectrum is the result of the soft photon diffusion upscattering (Comptonization) in the disk-like configuration (Compton cloud), the PDS is formed in the same configuration as a result of the diffusive propagation of high-frequency local driving perturbations. This solution is robust and generic. The result can find many applications where oscillations of boundary configurations are studied. Here we apply this solution to the particular astrophysical case of the disk oscillations.

The resulting model time signal as a linear combination of quite a few *related* exponential shots is in a good agreement with the observations. The observable PDS is perfectly fitted by a sum of LF and HF white-red noise power spectra. *This fact can be interpreted as an observational evidence of the presence of two independent components in the accretion flow.* One is related to the extended geometrically thin disk (LF PDS component) and the other - to the geometrically thick compact configuration (HF PDS component). Each of the white-red noise (WRN) components has two free parameters, the diffusion time scale t_0 and the viscosity index ψ . The value of the parameter t_0 has a physically plausible value for the viscous timescale of the disk-like configuration and ultimately is applied to the calculation of the Reynolds number of the accretion flow Re . In fact, the value of Re can be inferred if t_0 , ψ and QPO low frequency ν_L are known from observations (see Eq. 90).

In the observed power spectra (particularly in the intermediate state) we deal with two diffusion time scales, one $t_{C,0}$ is related to the inner compact region, presumably Compton cloud (sub-Keplerian disk, ADAF) and the other $t_{D,0}$ is related to a much larger disk. The diffusion time scale of the inner region is scaled with the mass of the central object and $t_{D,0}$ is scaled with the orbital period of the system. The diffusion time scale t_* (as the best-fit parameter of the Lorentzian) determines a high-frequency turnover in PDS (see Fig. 2). It may be related to the combined effect of the photon diffusion in the CC-wind configuration and high frequency (local) fluctuations in the accretion flow. More precise estimate of the time scale of the driving oscillation requires further investigation.

We present the broadband PDSs of black hole source Cyg X-1 in hard (Fig. 4) and soft (Fig. 6) states, illustrating the presence of LF and HF components in hards state and the absence of HF component ((or a weak HF) in the soft state. In Figures 2, 3 we show the evolution of LF and HF components in high frequency PDS of Cyg X-1. We also find that Cyg X-2 PDS also consists of LF and HF components (see Figure 11). The best-parameters

of the model allows us to determine the diffusion time scales of geometrically thin extended disk $t_{D,0}$ and geometrically thick configuration (Compton cloud) $t_{C,0}$. They differ by almost six orders of magnitude, namely $t_{D,0} \sim 0.7 \times 10^6$ s and $t_{C,0} \sim 0.8$ s. We infer the Reynolds numbers Re and related α_{SS} parameters of the CC flow for Cyg X-1 and Cyg X-2. We find they are quite similar for each source, namely Re is about 7.5 and α_{SS} is about 0.14.

LT appreciates productive questions by Marat Gilfanov, Ralph Fiorito, Martin Laming, and Demos Kazanas. VA acknowledges useful discussion with Marat Gilfanov and a partial support of this work from the program “the origin and evolution of stars and galaxies” of the Russian Academy of Science. NS thanks Craig Markwardt for outstanding software products. We also acknowledge the referee’s contribution in Discussion section.

A. Power spectrum of weakly correlated signals

If two signals $\Delta L_1(t)$ and $\Delta L_2(t)$ in the system are weakly correlated then the resulting power spectrum is a sum of the corresponding spectra Namely,

$$\int_0^\infty [\Delta L_1(t) + \Delta L_2(t)]^2 dt \approx \int_0^\infty [\Delta L_1^2(t) + \Delta L_2^2(t)] dt \quad (\text{A1})$$

Using Parseval's theorem for Fourier transforms, we obtain that

$$\int_0^\infty [\Delta L_1^2(t) + \Delta L_2^2(t)] dt = \int_0^\infty [||F_{x_1}(\omega)||^2 + ||F_{x_2}(\omega)||^2] d\omega. \quad (\text{A2})$$

where $F_{x_1}(\omega)$ and $F_{x_2}(\omega)$ are Fourier transforms of $\Delta L_1(t)$ and $\Delta L_2(t)$ respectively. Thus the energy per unit frequency, resulting power spectrum, $||F_{x_1+x_2}(\omega)||$ is a sum of two components

$$||F_x(\omega)|| = ||F_{x_1}(\omega)||^2 + ||F_{x_2}(\omega)||^2. \quad (\text{A3})$$

B. Diffusion of the driving perturbations. Mathematical details

B.1. Solution of Eq. (2) for the general case of the spatial and time dependent distribution of driving perturbation

The diffusion equation for the time variable quantity $W(R, t)$, related to the surface density can be written as (compare with Eq. 2):

$$\frac{\partial W}{\partial t} = \Lambda_{\mathbf{R}} W + \Phi(t, R). \quad (\text{B1})$$

The solution of equation (B1) with homogeneous initial condition $W(R, 0) = 0$ can be presented using the Green's function $G(R, \xi, t)$ derived by W01 (see Eq. 21 there), namely, $G(R, \xi, t) = V_{x_0}(x, t)/[\nu(x_0)/\pi]$ (where $x = R^{1/2}$ and $x_0 = \xi^{1/2}$) . Thus the solution is (compare with Eq. 3)

$$W(R, t) = \int_0^t \int_{R_{in}}^{R_0} G(R, \xi, t - t') \Phi(t', \xi) d\xi dt'. \quad (\text{B2})$$

Then a Fourier transform of $W(R, t)$ is

$$F_W(R, \omega) = \int_{R_{in}}^{R_0} F_G(R, \xi, \omega) F_\Phi(\xi, \omega) d\xi. \quad (\text{B3})$$

Without any loss of generality we assume that the local driving perturbations are damped quasiperiodic oscillations, namely

$$\Phi(t, \xi) = A_\Phi f(\xi) \exp(-\frac{1}{2}\Gamma_{dr}t + i\omega_{dr}t) \quad (\text{B4})$$

where ω_{dr} and the damping factor are in principle functions of ξ , A_Φ is a numerical factor related to an amplitude of the driving quasiperiodic oscillations. In this case a Fourier transform of $\Phi(t, \xi)$ is

$$F_\Phi(\xi, \omega) = \frac{A_\Phi f(\xi)}{\Gamma_{dr}/2 + i(\omega - \omega_{dr})}. \quad (\text{B5})$$

For a product of continuous functions $g_1(\xi)$, $g_2(\xi)$ and $g_3(\xi)$ the mean value theorem states that

$$\int_a^b g_1(\xi)g_2(\xi)g_3(\xi)d\xi = g_3(\xi_*) \int_a^b g_1(\xi)g_2(\xi)d\xi \quad (\text{B6})$$

where ξ_* is between a and b . Using this mean value theorem and formula (B5) for $F_\Phi(\xi, \omega)$ we can present Eq. (B3) as

$$F_W(R, \omega) = \frac{A_\Phi}{\Gamma_{dr}(\xi_*)/2 + i[\omega - \omega_{dr}(\xi_*)]} \int_{R_{in}}^{R_0} F_G(R, \xi, \omega) f(\xi) d\xi \quad (\text{B7})$$

where ξ_* is some mean value of ξ between R_{in} and R_0 . The integral in the right hand side of equation (B7) is the Fourier transform of the solution of the initial value problem $X(\xi, t)$ for the homogeneous diffusion equation (4) with the initial function $X(\xi, 0) = f(\xi)$:

$$F_W(R, \omega) = \frac{1}{\Gamma_{dr}(\xi_*)/2 + i[\omega - \omega_{dr}(\xi_*)]} F_X(R, \omega). \quad (\text{B8})$$

Using Eqs. (B8), (19), (20) we obtain the Fourier transform of the resulting X-ray signal due to the diffusion of the driving perturbations

$$F_x(\omega) = 3\pi\varepsilon_{eff} \frac{\partial[x\hat{\nu}F_W(\omega, x^2)]}{\partial x} \Big|_{x=0} \quad (\text{B9})$$

Then the power spectrum $\|F_x(\omega)\|^2$ is a product

$$\|F_x(\omega)\|^2 = \frac{A_\Phi^2 \|F_Y(\omega)\|^2}{[\omega - \omega_{dr}(\xi_*)]^2 + [\Gamma_{dr}(\xi_*)/2]^2} \quad (\text{B10})$$

where $Y(t)$ is determined by formula (20). Comparison of formulas (22) and (B10) leads to the conclusion that the value of ω_{dr} in formula (22) is some mean value of the rotational frequency of the local quasiperiodic oscillations. This frequency, likely related to the local Keplerian frequency is much higher than the diffusion frequency of the disk-like configuration (see §3).

B.2. A relation between the total power of the driving (source) oscillations and resulting power due to diffusion of the driving perturbations

We can estimate the integrated power of $\|F_x(\omega)\|^2$ if we estimate that for $\|F_{dr}(\omega)\|^2$ and $\|F_Y(\omega)\|^2$. But from Parseval 's theorem of Fourier transform we know that

$$\int_0^\infty \|F_Y(\omega)\|^2 dt = \int_0^\infty Y^2(t) dt. \quad (\text{B11})$$

The integral of $Y^2(t)$ in Eq. (B11) can be evaluated using the integral of $Y(t)$. It is easy to show that

$$\int_0^\infty Y(t) dt = \varepsilon_{eff} \int_0^{R_0} f(R) 2\pi R dR = 1. \quad (\text{B12})$$

To derive Eq. (B12) we integrate Eq. (12) over t (from 0 to ∞) and over x (from 0 to x_0) and we also use Eqs. (13), (17) and the outer boundary condition $\partial\mathcal{X}/\partial x(x_0, t) = 0$ (see W01).

When the driving perturbations are distributed in the disk according to the first eigenfunction of the space operator of the diffusion equation (2) then $Y(t) = t_* \exp(-t/t_*)$ (see more details in §3). Here t_* is related to the diffusion time scale in the disk t_0 . Fore example, $t_* = 4t_0/\pi^2$ for the linear dependence of viscosity $\hat{\nu}$ vs radius, $\psi = 2$ [see an exponent of the first term in series (45)].

In this case we can calculate exactly the integral

$$\int_0^\infty Y^2(t) dt = \frac{1}{2t_*} \quad (\text{B13})$$

and then from Parseval 's theorem of Fourier transform we obtain that

$$\int_0^\infty \|F_Y(\omega)\|^2 d\omega = \int_0^\infty Y^2(t) dt = \frac{1}{2t_*}. \quad (\text{B14})$$

In the general case of the spatial distribution this can be estimated as follows

$$\int_0^\infty Y^2(t) dt \geq \left[\int_0^\infty Y(t) dt \right]^2 / \int_0^{\hat{D}t_*} dt \geq \frac{1}{\hat{D}t_*} = \frac{1}{Dt_0}. \quad (\text{B15})$$

using Hölder's inequality. Here $\hat{D} \gtrsim 2$ (compare with Eq. B13). To derive inequality (B15) we also use the asymptotic behavior of $Y(t)$, namely $Y(t) \propto \exp(-t/t_*)$ for $t \gg t_*$ (see details in §3). Because $t_* \approx t_0/2.5$ (see Eq. 45) we can replace a product $\hat{D}t_*$ in Eq. (B15) by Dt_0 where $D \gtrsim 1$. Then we find that

$$\int_0^\infty \|F_Y(\omega)\|^2 d\omega = \int_0^\infty Y^2(t) dt \geq \frac{1}{Dt_0}. \quad (\text{B16})$$

Finally Eqs (21), (B16) gives us the integrated total power of the resulting signal

$$P_x = \int_0^\infty ||F_x(\omega)||^2 d\omega \sim \frac{1}{D\mathcal{Q}} \frac{P_{dr}}{\omega_{dr}t_0} \quad (\text{B17})$$

where $\mathcal{Q} = \omega_{dr}/\Delta\omega \gtrsim 1$ is a quality of factor, $\Delta\omega$ is a HMF_W of $||F_x(\omega)||^2$. To obtain equation (B17) we also use the mean value theorem.

$$\int_0^\infty ||F_{dr}(\omega)||^2 ||F_Y(\omega)||^2 d\omega = ||F_{dr}(\omega_*)||^2 \int_0^\infty ||F_Y(\omega)||^2 d\omega \quad (\text{B18})$$

where

$$||F_{dr}(\omega_*)||^2 \sim P_{dr}/(\mathcal{Q}\omega_{dr}). \quad (\text{B19})$$

C. Power spectrum. General treatment

The Fourier transform of $Y(t)$ is calculated as follows (see e.g. Eq. 9, and Eqs. 45, 57):

$$F_Y(\omega) = \sum_{k=1}^{\infty} \frac{A_k}{i\omega + \lambda_k^{-2}}. \quad (\text{C1})$$

Then the power spectrum is

$$||F_Y(\omega)||^2 = F_Y(\omega) \overline{F_Y(\omega)} = \sum_{k=1}^{\infty} \frac{A_k}{i\omega + \lambda_k^{-2}} \sum_{m=1}^{\infty} \frac{A_m}{-i\omega + \lambda_k^{-2}}. \quad (\text{C2})$$

Because for any complex values a and b ,

$$a\bar{a} + b\bar{b} = |a|^2 + |b|^2 \geq (a\bar{b} + \bar{a}b) \quad (\text{C3})$$

[where in our case $a = A_k/(i\omega + \lambda_k^{-2})$ and $b = A_m/(i\omega + \lambda_k^{-2})$] we can evaluate $||F_Y(\omega)||^2$ using Eq. (C2) as follows

$$||F_Y(\omega)||^2 \leq 2 \sum_{k=1}^{\infty} \frac{A_k^2}{\omega^2 + \lambda_k^{-4}}. \quad (\text{C4})$$

D. Fourier transform of the FRED type fluctuation $Y(t)$

In section §3.3 we introduce the FRED type of the signal $Y(t)$ (see Eq. 70). The Fourier transforms of $Y(t)$ in this case is expressed through the modified Bessel functions see PBM81, 2.3.16):

$$F_Y(\omega) \propto (C_0 I_0 + C_1 I_1), \quad (\text{D1})$$

where

$$I_j = \left(\frac{\pi}{2}\right)^{1/2} \frac{2^{1-\alpha_j} t_0^{\alpha_j} \exp[-i(\alpha_j + 1/2)\varphi/2]}{\rho^{\alpha_j/2+1/4}} \exp[-\rho^{1/2} \cos(\varphi/2) - i\rho^{1/2} \sin(\varphi/2)] \quad \text{for } j = 0, 1 \quad (\text{D2})$$

where $\alpha_0 = 1$ and $\alpha_1 = 1/2 - \gamma$,

$$\rho = (z_1^4 + \omega^2 t_0^2)^{1/2}, \quad (\text{D3})$$

$$\varphi = \arcsin(\omega t_0 / \rho). \quad (\text{D4})$$

To present integrals I_j by formula (D2) we approximate the modified Bessel functions [e.g. Abramovitz & Stegun (1970)]

$$K_{\alpha_j}(w) \approx \left(\frac{\pi}{2}\right)^{1/2} \exp(-w)/w^{1/2},$$

where

$$w = \rho^{1/2} [\cos(\varphi/2) + i \sin(\varphi/2)],$$

because $|w|$ in $K_{\alpha_j}(w)$ is always greater than 1. In fact, W01 showed that $z_1 > 1$ but $w \gtrsim z_1^2$.

E. The Eddington luminosity limit in the disk and mass outflow in the wind

The critical \dot{M}_d^{crit} to launch the wind at a given disk radius R is determined by an equality of the radiation pressure and gravitational force in a given annulus between R and $R + dR$, namely

$$\frac{\sigma(R) Q_d^{crit}(R)}{c} = m_p \left(\frac{H}{R}\right) \frac{GM}{R^3}. \quad (\text{E1})$$

Here

$$Q_d^{crit}(R) = \frac{3}{8\pi} \frac{GM \dot{M}_d^{crit}}{R^3} [1 - (R_*/R)^{1/2}] \quad (\text{E2})$$

is the disk luminosity per cm^2 in the annulus between R and $R + dR$ (see SS73), R_* is the central object radius, that is 3 Schwarzschild radii for BH and the NS radius for NS; $\sigma(R)$ is an effective plasma cross section which equals to the electron Thomson cross-section σ_T if the disk plasma is fully ionized, otherwise $\sigma(R) > \sigma_T$ (see e.g. Proga 2005); H is a geometrical half-thickness of the disk; M is a mass of the central object, BH mass or NS mass for BH and NS cases respectively.

Thus we obtain using Eqs (E1-E2) that

$$\dot{M}_d^{crit}(R) = \frac{8\pi}{3} R \left(\frac{H}{R}\right) \frac{m_p c}{\sigma(R)} \frac{1}{[1 - (R_*/R)^{1/2}]}. \quad (\text{E3})$$

If H/R is constant through the disk (see SS73) then $\dot{M}_d^{crit} \propto R/\sigma(R)$. In this case the critical mass accretion rate $\dot{M}_{out,d}^{crit}$ at the outer disk radius R_{out} is much higher than that $\dot{M}_{in,d}^{crit}$ at the innermost disk radius R_{in} , namely

$$\frac{\dot{M}_{out,d}^{crit}}{\dot{M}_{in,d}^{crit}} = \frac{R_{out}}{R_{in}} \frac{\sigma_T}{\sigma(R_{out})} \frac{[1 - (R_*/R_{in})^{1/2}]}{[1 - (R_*/R_{out})^{1/2}]} \quad (\text{E4})$$

The disk works as a filter that does not allow to supply \dot{M} higher than $\dot{M}_d^{crit}(R_{in})$ to the innermost part of the disk. Much larger fraction of the total mass inflow is converted to the mass outflow when the mass supply to the disk from the companion is very high. This likely occurs in Cyg X-1, Cyg X-2 and Sco X-1 cases.

The next question which should be addressed is what is the total luminosity of the disk L_d^{crit} if at any annulus the disk emits at the Eddington limit (see Eq. E3)? In order to answer to this question we should integrate Q_d^{crit} over the radius, namely

$$L_{d,tot}^{crit} = \int_{R_{in}}^{R_{out}} Q_d^{crit}(R) 4\pi R dR = 4\pi GM \left(\frac{H}{R}\right) \frac{m_p c}{\sigma_T} \int_{R_{in}}^{R_{out}} \frac{\sigma_T}{\sigma(R)} \frac{dR}{R}. \quad (\text{E5})$$

Because

$$\int_{R_{in}}^{R_{out}} \frac{\sigma_T}{\sigma(R)} \frac{dR}{R} \approx \frac{\sigma_T}{\sigma(R_{out})} \ln(R_{out}/R_{in}) \quad (\text{E6})$$

and by definition

$$L_{\text{Edd}} = \frac{4\pi GM m_p c}{\sigma_T} \quad (\text{E7})$$

we have that

$$L_{d,tot}^{crit} = \left[\left(\frac{H}{R}\right) \frac{\sigma_T}{\sigma(R_{out})} \ln(R_{out}/R_{in}) \right] L_{\text{Edd}}. \quad (\text{E8})$$

On the other hand using Eqs. (E2, E3) we obtain that the disk luminosity $L_{d,in}^{crit}$ with the constant $\dot{M}_{in,d}^{crit}$ is

$$L_{d,in}^{crit} = \int_{R_{in}}^{R_{out}} Q_d^{crit}(R_{in}) 4\pi R dR \sim \left(\frac{H}{R}\right) L_{\text{Edd}}. \quad (\text{E9})$$

Thus we expect the saturation of the total disk luminosity with the mass supply to the disk because

$$\frac{L_{d,tot}^{crit}}{L_{d,in}^{crit}} \sim 2 \times \left[\frac{\ln(R_{out}/R_{in})}{10} \right] \left[\frac{\sigma_T/\sigma(R_{out})}{0.2} \right]. \quad (\text{E10})$$

Here we use representative values of the ratios $R_{out}/R_{in} \sim 10^4$ (see e.g. SS73) and $\sigma_T/\sigma(R_{out}) \sim 0.2$ (Proga 2005).

Now we can calculate the total mass outflow rate in the sources in which mass accretion supply from companion is very high, i.e about $\dot{M}_d^{crit}(R_{out})$. Because $\dot{M}_d^{crit}(R) < \dot{M}_d^{crit}(R+dR)$

(see Eq. E3) the surplus (overflow) $\Delta\dot{M}_d^{crit}(R)$ in the annulus $(R, R+dR)$ emerges as outflow there, i.e. the mass outflow rate is $\Delta\dot{M}_{outflow}^{crit}(R) = \Delta\dot{M}_d^{crit}(R)$. Consequently, the total mass outflow rate from the disk is

$$\dot{M}_{outflow}^{crit} = \int_{R_{in}}^{R_{out}} \Delta\dot{M}_d^{crit}(R)dR \sim \dot{M}_d^{crit}(R_{out}) \quad (\text{E11})$$

which is much higher than the critical mass accretion rate at inner disk radius

$$\frac{\dot{M}_{outflow}^{crit}}{\dot{M}_d^{crit}(R_{in})} \sim \frac{R_{out}}{R_{in}} \gg 1. \quad (\text{E12})$$

The Thomson optical depth of outflow τ_W with a constant velocity v can be calculated using the continuity equation

$$\dot{M}_{outflow}^{crit} = 4\pi R^2 n \sigma_T m_p v \quad (\text{E13})$$

and Eq. (E11), namely

$$\tau_W = \int_{R_{out}}^{\infty} n \sigma_T dR = \frac{\dot{M}_{outflow}^{crit} \sigma_T}{4\pi m_p v} \int_{R_{out}}^{\infty} \frac{dR}{R^2}. \quad (\text{E14})$$

Finally we obtain using Eqs. (E3), (E11) and (E14) that

$$\tau_W = \frac{\dot{M}_{outflow}^{crit} \sigma_T}{4\pi m_p v R_{out}} = \frac{2}{3} \frac{H}{R} \frac{\sigma_T}{\sigma(R)} \frac{c}{v} \quad (\text{E15})$$

and thus $\tau_W \gtrsim 1$ for typical values of $H/R \sim 0.1$, $\sigma_T/\sigma(R) \sim 0.2$ and $v/c \sim (R_{in}/R_{out})^{1/2} \sim 0.01$. To evaluate the wind velocity v we use a formula for the wind terminal velocity derived in Rybicki & Lightman (1979) (see Chapter 1 there) and the value of $R_{out}/R_{in} \sim 10^4$.

REFERENCES

- Abramowitz, M., & Stegun, I. 1970, *Handbook of Mathematical Functions*, Dover Publications, New York
- Averalo, P. & Uttley, P. 2006, MNRAS, in press
- Chandrasekhar, S. 1961, *Hydrodynamics and Hydromagnetic Stability*, Oxford: Oxford at the Caredon Press
- Chakrabarti, S.K. & Titarchuk, L. G. 1995, ApJ, 455, 623
- Churazov, E., Gilfanov, M., & Revnivtsev, M. 2001, MNRAS, 321, 759
- Gies, D.R. et al. 2003, ApJ, 583, 424
- Gilfanov, M., & Arefiev, V. 2006, MNRAS, accepted, (astro-ph/0501215) (GA06)
- Grimm, H.-J., Gilfanov, M., & Sunyaev, R. 2002, A&A, 391, 923
- Kalemci, E 2003, PhD Thesis, (CASS/UCSD) (2002 BAAS, 34, 1206)
- King, A.R., Pringle, J.E., West, R.G., & Livio, M. 2004, MNRAS, 348, 111 (K04)
- Kotov, O., Churazov, E., & Gilfanov, M. 2001, MNRAS, 327, 799
- Laurent, P. & Titarchuk, L. 1999, ApJ, 511, 289 (LT99)
- Lyubarskii, Yu., E. 1997, MNRAS, 292, 679 (L97)
- Mayer, M. & Pringle, J.E. 2006, MNRAS, 368, 379 (MP06)
- Narayan, R., & Yi, I. 1997, ApJ, 428, L13
- Proga, D. 2005, ApJ, 630, L9
- Prudnikov, A. P., Bruchkov, Yu. A., & Marichev, O. I. 1981, *Integrals and Series* (Moscow: Nauka) (PBM01)
- Remillard, R. A. & McClintock, J. E. 2006, ARA&A, vol. 44, 49
- Revnivtsev, M., Gilfanov, M., & Churazov, E. 2000, A&A, 363, 1013
- Rybicki, G.B. & Lightman, A.P. 1979, *Radiative Processes in Astrophysics*, A Wiley-Interscience Publications, New York

- Shakura, N. I. & Sunyaev, R. A. 1973, *A&A*, 24, 337 (SS73)
- Shaposhnikov, N. & Titarchuk, L. 2006, *ApJ*, 643, 1098 (ST06)
- Smith, D. M.; Heindl, W. A.; Swank, J. H. 2002, *ApJ*, v. 569, p. 362
- Sunyaev, R.A. & Titarchuk, L.G. 1985, *A&A*, 143, 374 (ST85)
- Sunyaev, R.A. & Titarchuk, L.G. 1980, *A&A*, 86, 121 (ST80)
- Swank, J. H. 1999, *Nucl. Phys. B - Proc. Suppl.*, 69, 12, v. 569, p. 362
- Titarchuk, L. 2003, *ApJ*, 591, 354
- Titarchuk, L.G., Cui, W., & Wood, K.S., 2002, *ApJ*, 576, L49 (TCW02)
- Titarchuk, L.G., Bradshaw, C.F., & Wood, K.S. 2001, *ApJ*, 560, L45 (TBW01)
- Titarchuk, L.G. & Fiorito, R. 2004, *ApJ*, 612, 988 (TF04)
- Titarchuk, L. G., Mastichiadis, A., & Kylafis, N. D. 1997, *ApJ*, 487, 834
- Titarchuk, L. & Shaposhnikov, N. 2005, *ApJ*, 626, 298
- Titarchuk, L. & Shrader, C.R. 2005, *ApJ*, 623, 362
- Titarchuk, L., & Zannias, T., 1998, *ApJ*, 493, 863
- Turner, M., Smith, A., & Zimmerman, H. 1981, *Space Science Rev.*, 30, 513
- Uttley, P., McHardy, I.M., & Vaughan, S. 2005, *MNRAS*, 359, 345
- Uttley, P. 2004, *MNRAS*, 347, L61
- Vignarca, F., Migliari, S., Belloni, T., Psaltis, D., & van der Klis, M. 2003, *A&A*, 397, 729 (V03)
- Wood, K. S., Titarchuk, L., Ray, P.S., et al. 2001, *ApJ*, 563, 246 (W01)

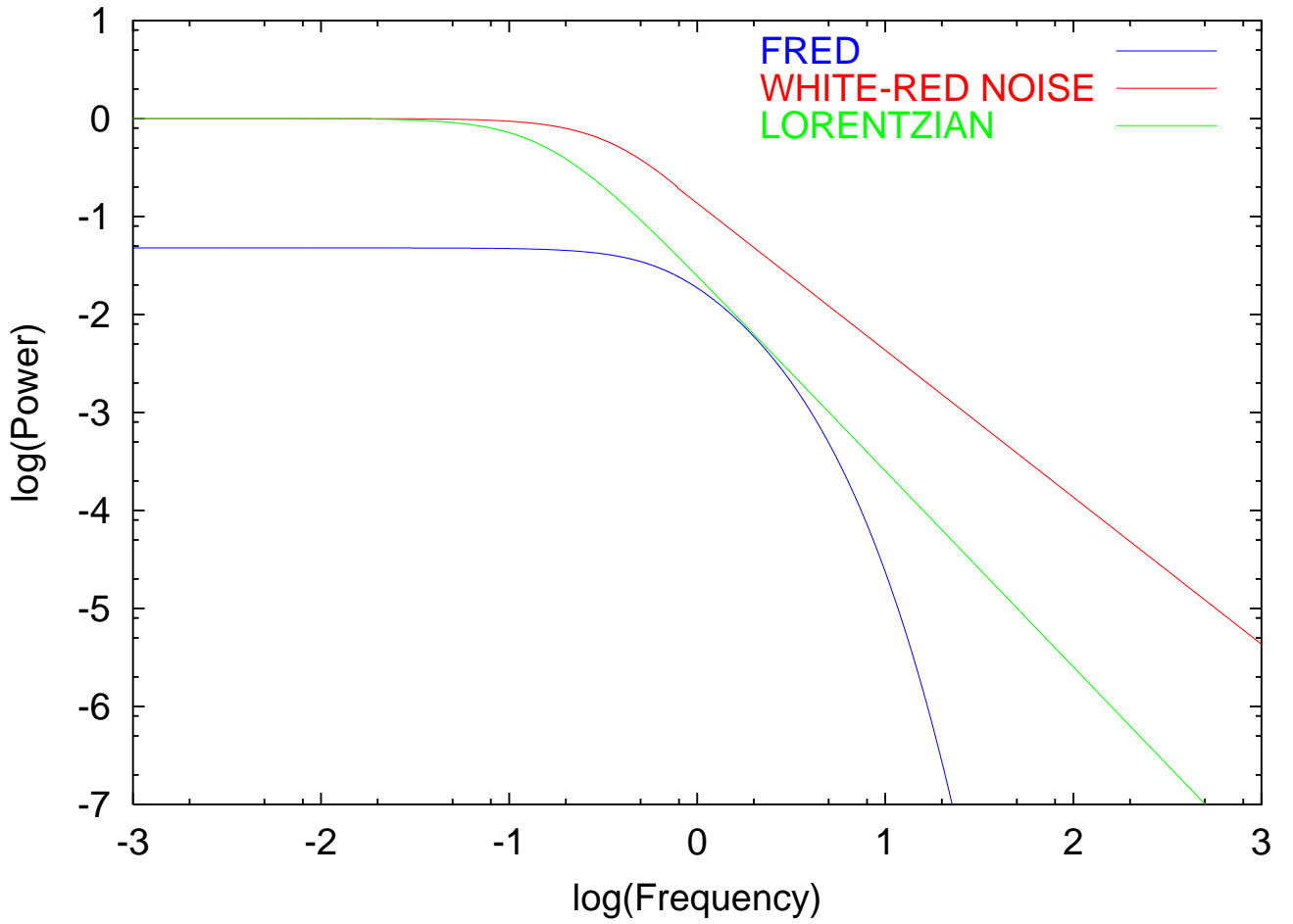


Fig. 1.— Examples of PDS models: PDS of fast rise and exponential decay (FRED) (blue line), PDS of white-red noise (red line) and Lorentzian PDS (green line).

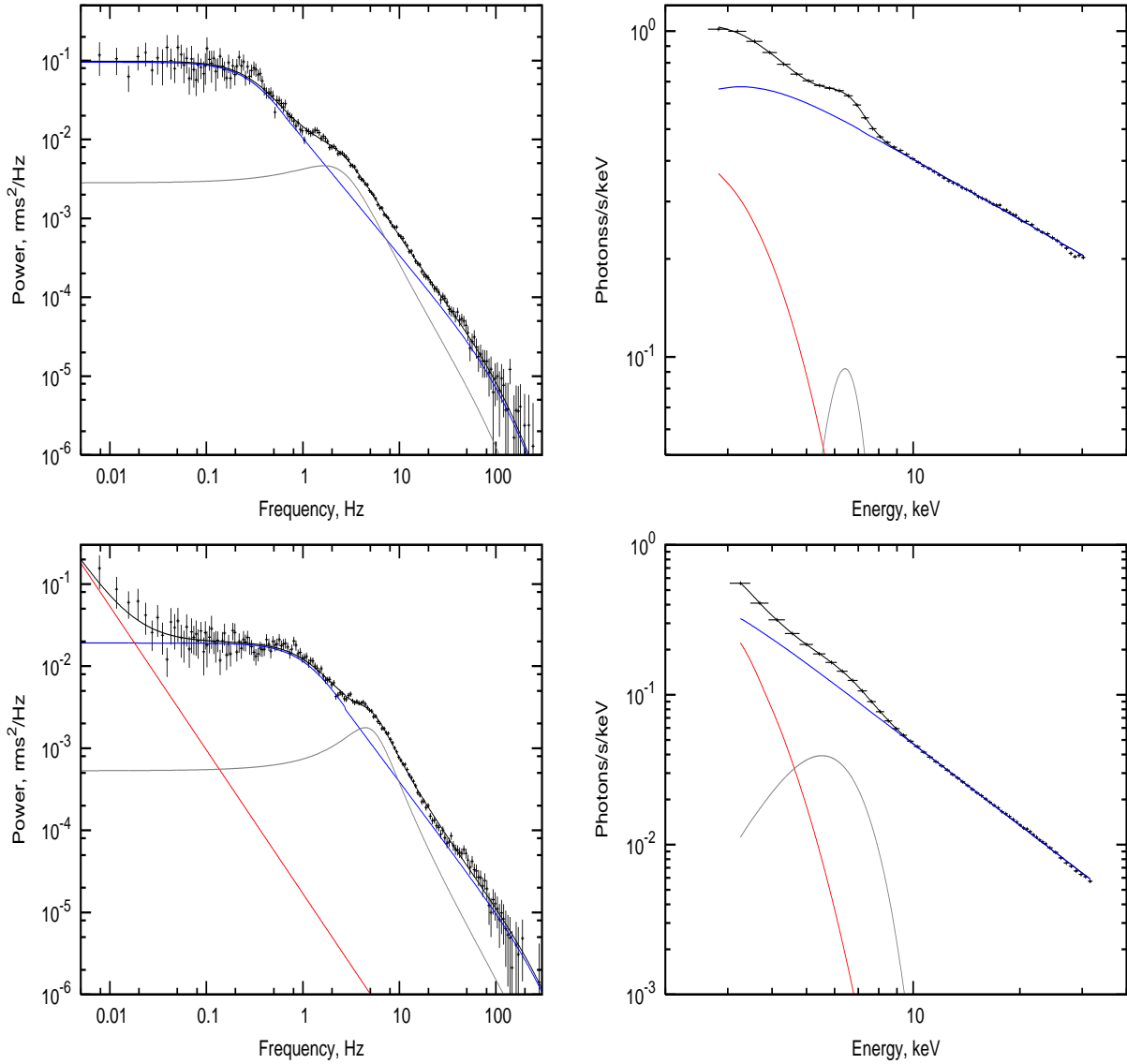


Fig. 2.— Cyg X-1: Observable power spectrum (PDS) (left panel) vs photon spectrum (right panel) from observations 40099-01-05-00(upper panels) and 50119-01-04-01(lower panel). The first observation is a pure low/hard state with no LF WRN component in the PDS. During the second observation the source energy spectrum is still hard, but LF WRN is already detectable. Data points are shown with error bars. PDS is fitted by a product of the sum of LF and HF WRN power spectra and zero-centered Lorentzian (see formula 85). We also use Lorentzians to fit QPO features. The model fit χ^2 are shown in Table 1. Black line is for the resulting PDS as red and blue lines present LF and HF components respectively. Photon spectrum is fitted by BMC+GAUSSIAN model. The resulting model spectrum is shown in black, while red and blue curves present thermal and Comptonized components respectively. Grey line presents GAUSSIAN of K α line located at 6.4 keV.

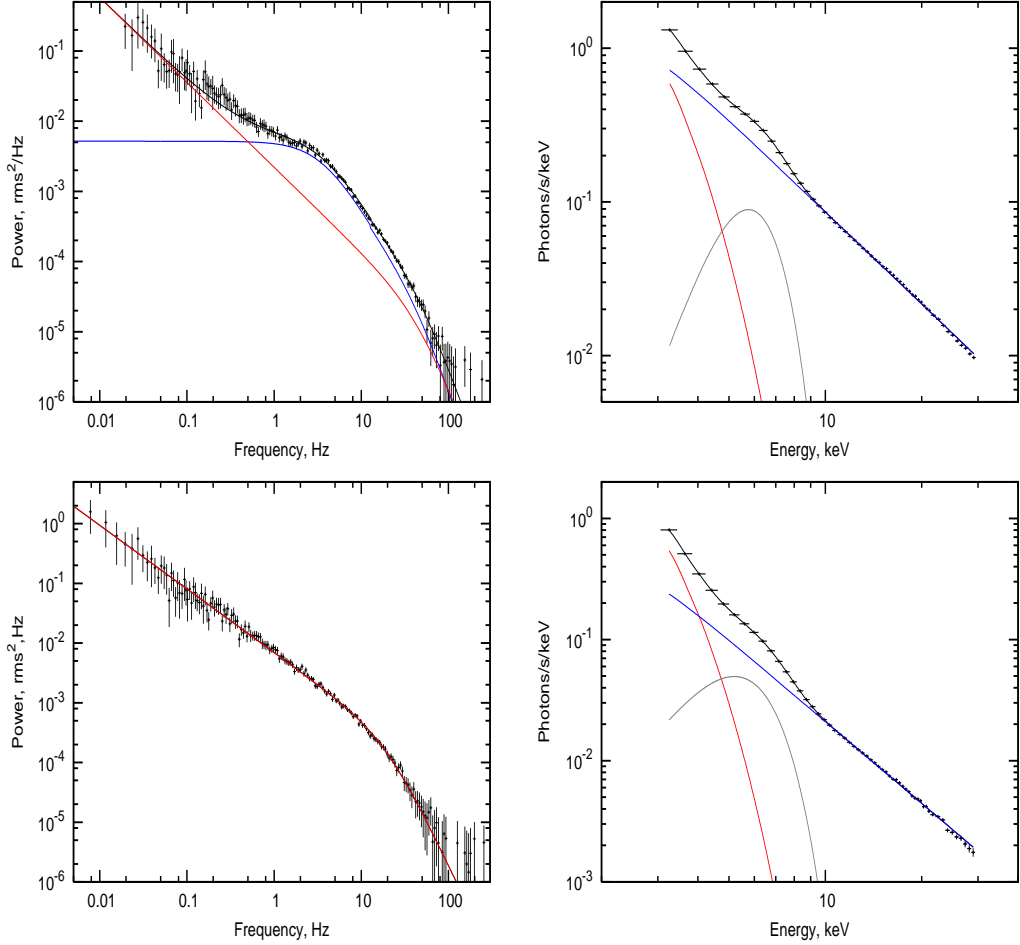


Fig. 3.— The same as Figure 2 but for observations 50109-01-01-00 (upper panels) and 60090-01-14-01 (lower panels). The first observation is taken during the intermediate state just before the transition to high/soft state, which is presented by the second observation. No HF WRN is present in PDS during high/soft state.

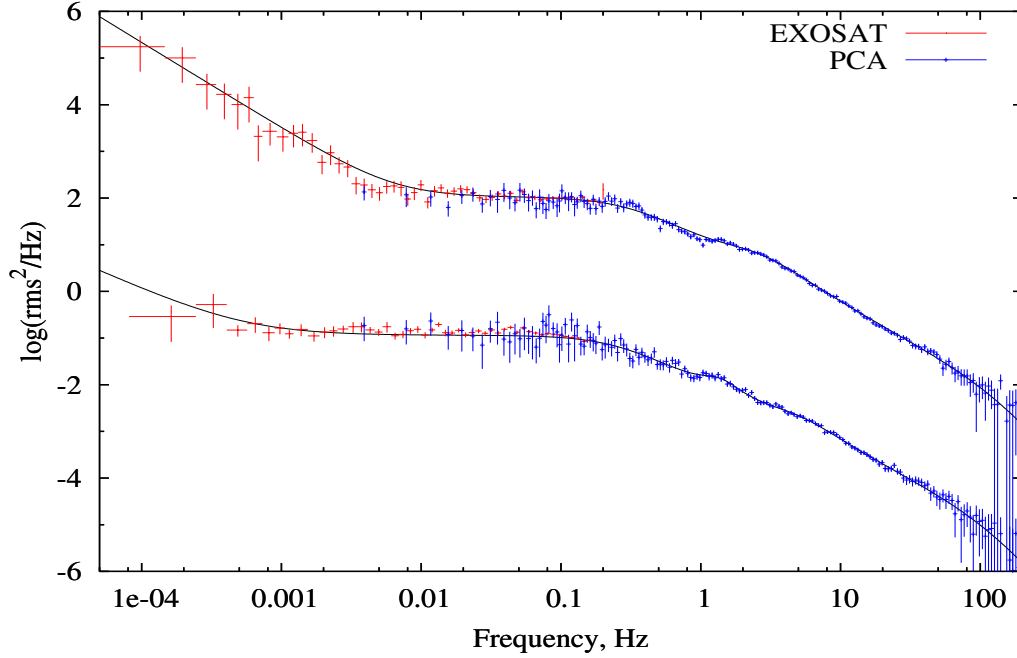


Fig. 4.— Two composite PDSs: EXOSAT spectra with matching high frequency PCA PDS. PCA data for lower PDS is taken from observation ID 40099-01-03-01 and for upper PDS - from observation ID 40099-01-05-00. Data are fitted by LF-HF diffusion model: $\chi^2/N_{dof} = 250.1/267 = 0.94$, $\psi_{CC} = 2.32 \pm 0.12$, $t_{0,C} = 1.8 \pm 0.3$, $\psi_D = 2.5$ (fixed) and $\chi^2/N_{dof} = 278.5/267 = 1.04$, $\psi_{CC} = 2.07 \pm 0.7$, $t_{0,C} = 1.24 \pm 0.12$, $\psi_D = 0.3 \pm 0.3$ (fixed) for lower and upper panels fits respectively.

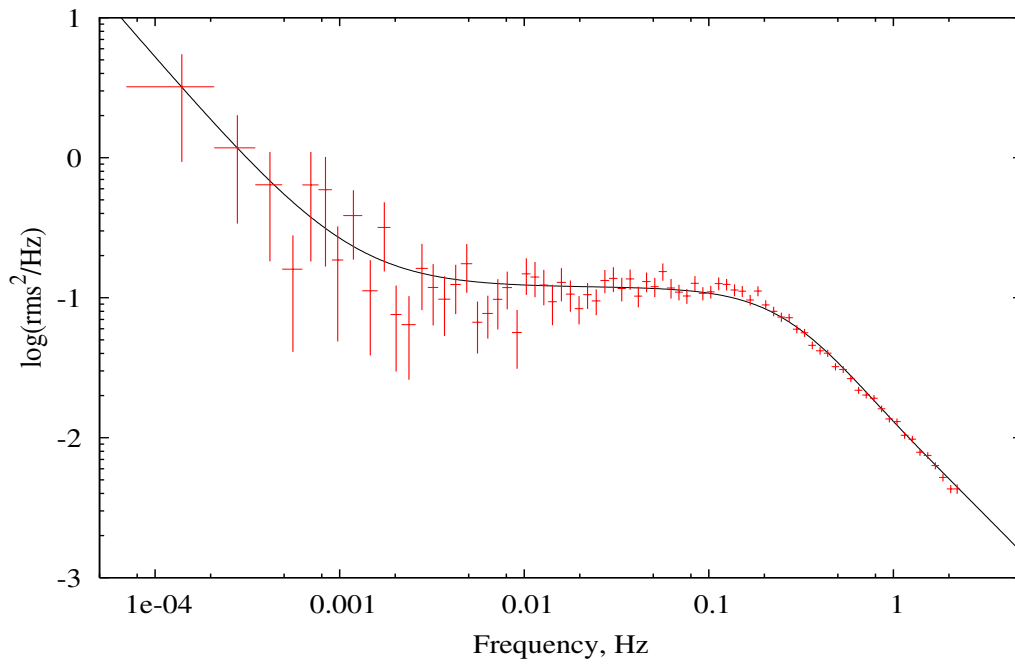


Fig. 5.— High time-resolution EXOSAT/ME PDS of Cyg X-1 from the data collected on 24 July 1984 with high time resolution of 0.2 sec. Data are fitted by LF-HF diffusion model: $\chi^2/N_{dof} = 94.5/74 = 1.27$, the best-fit parameters $\psi_{CC} = 2.48 \pm 0.02$, $\psi_D = 1.8 \pm 0.3$, $t_{0,C} = 2.0 \pm 0.2$ s.

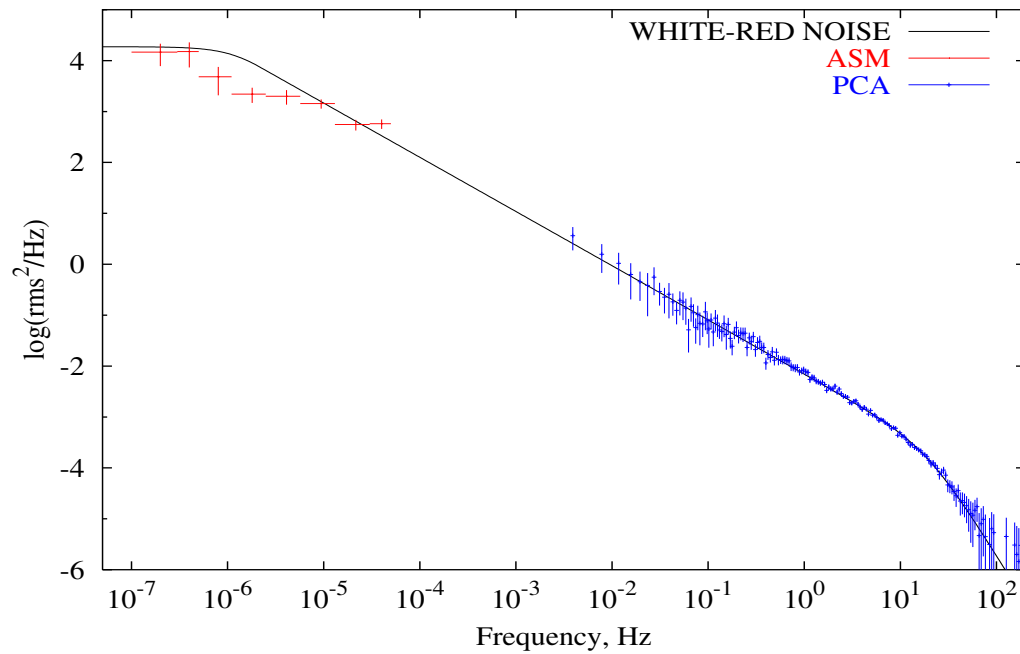


Fig. 6.— The composite soft state PDS is made by PCA (blue) and ASM (red) PDSs. The PCA PDS is for ObsID 50110-01-52-00 (see Table 1 and the bottom panel of of Fig. 3). Data are fitted by LF-HF diffusion model: $\chi^2/N_{dof} = 184/228 = 0.81$, the best -fit parameters $t_{0,D} = (6 \pm 1.7) \times 10^5$ s, $\psi_D = 2.93 \pm 0.01$.

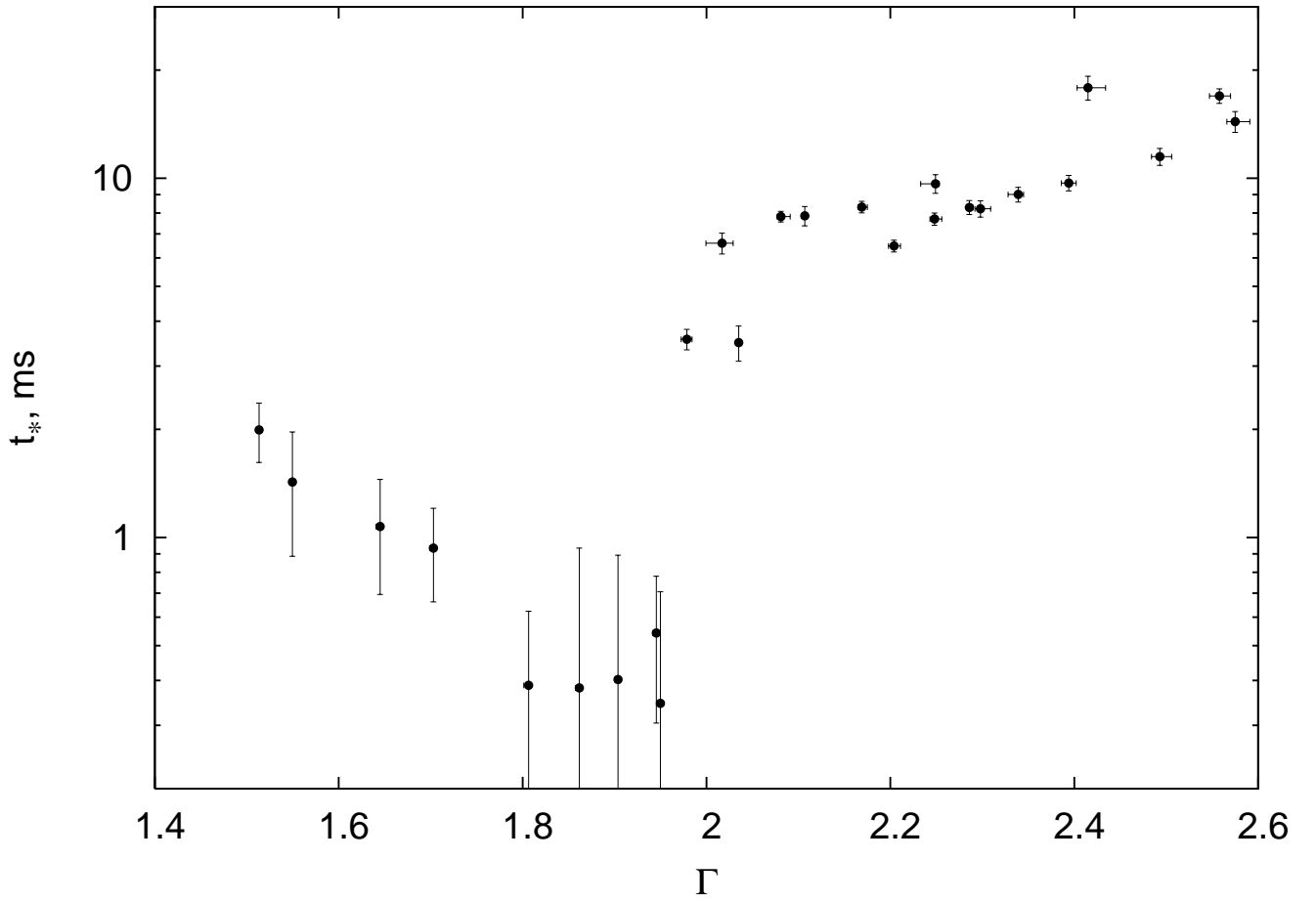


Fig. 7.— Cyg X-1: HF photon diffusion PDS (Lorentzian): the best-fit photon diffusion time t_* vs photon index Γ .

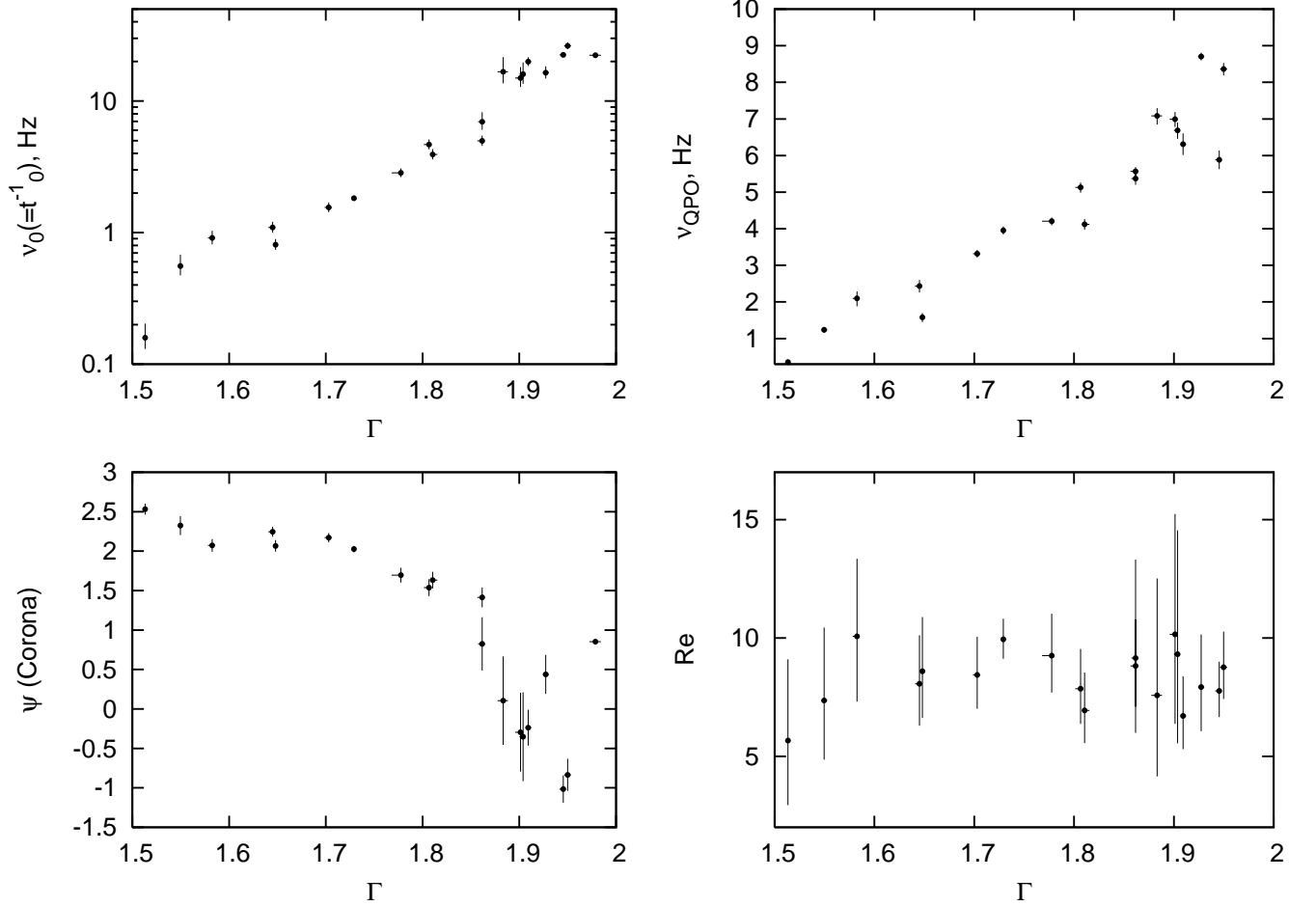


Fig. 8.— Cyg X-1: HF white-red noise component: the best-fit diffusion frequency $\nu_0 = t_0^{-1}$ vs Γ (upper left panel), QPO low frequency ν_{QPO} (ν_L) vs Γ (right upper panel), the best-fit index of the viscosity distribution ψ vs Γ (lower left panel) and inferred Reynolds number Re (using t_0 , ν_L , ψ , and Eq.90) vs Γ (lower right panel).

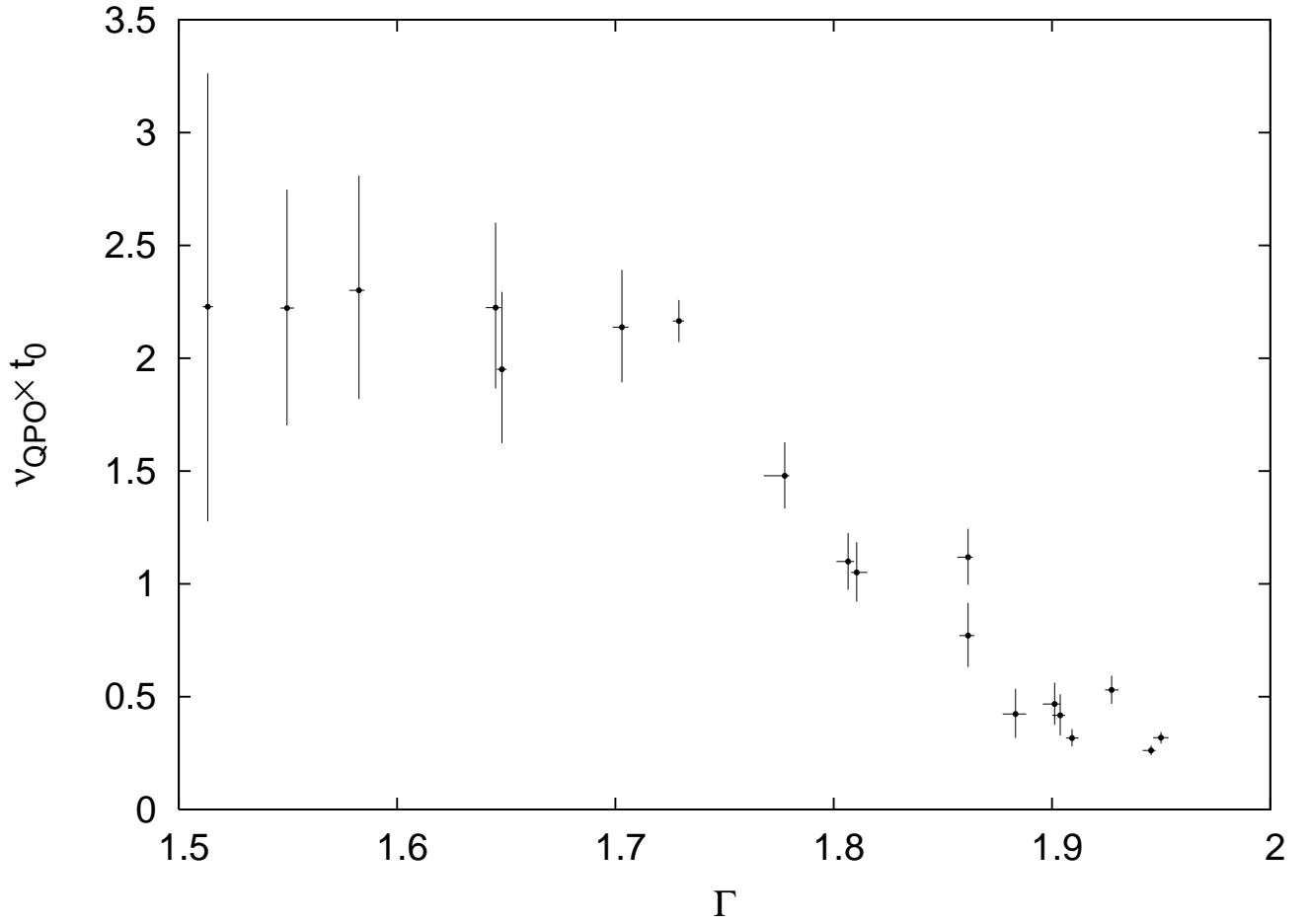


Fig. 9.— Cyg X-1: a product of QPO low frequency ν_{QPO} (ν_L) and the best-fit diffusion time of HF WRN t_0 vs Γ . Decrease of $\nu_{QPO} \times t_0$ with Γ implies that Compton cloud contracts when the source evolves to the softer states.

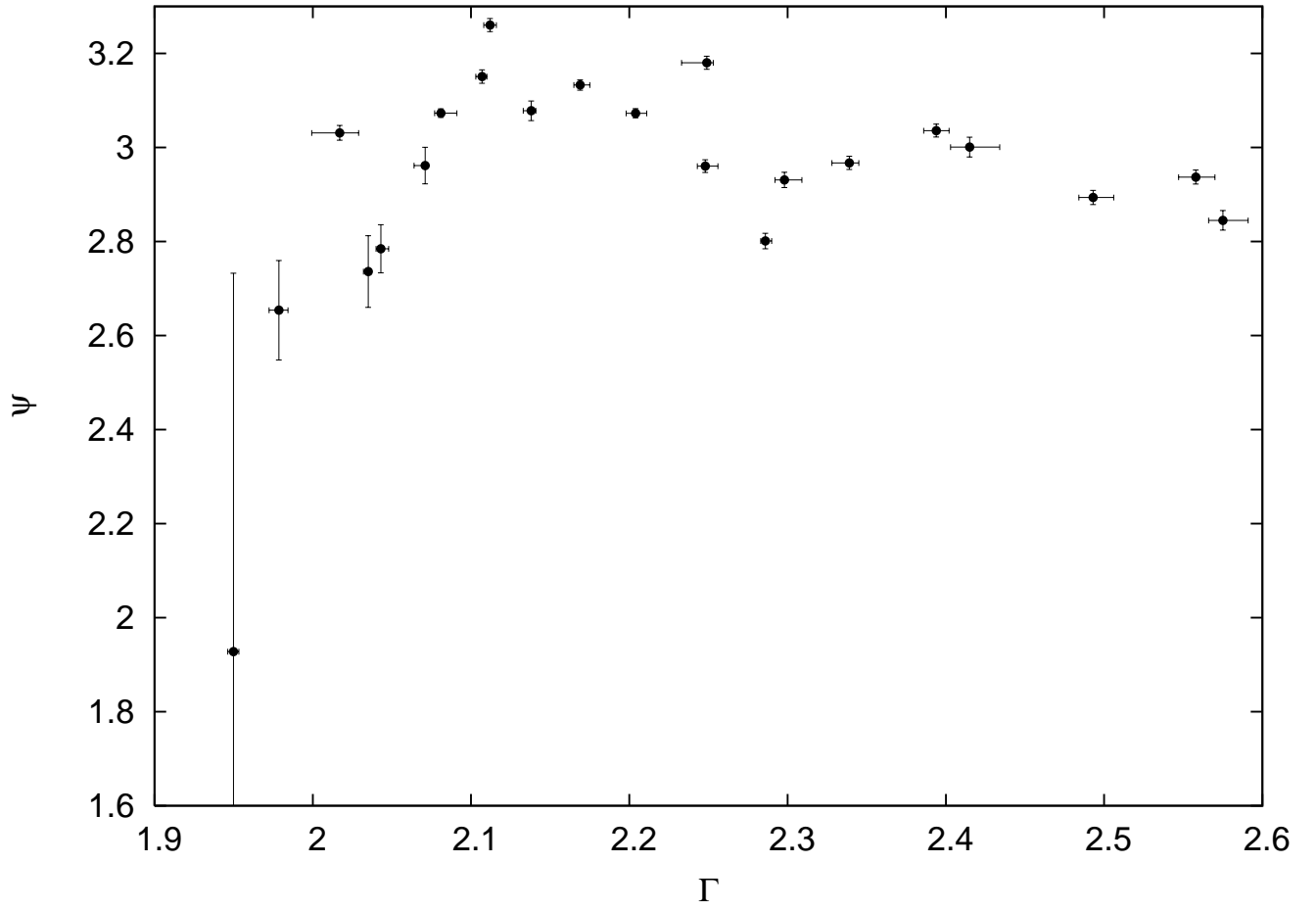


Fig. 10.— Cyg X-1: LF white-red noise component: The best-fit viscosity index ψ vs photon index Γ .

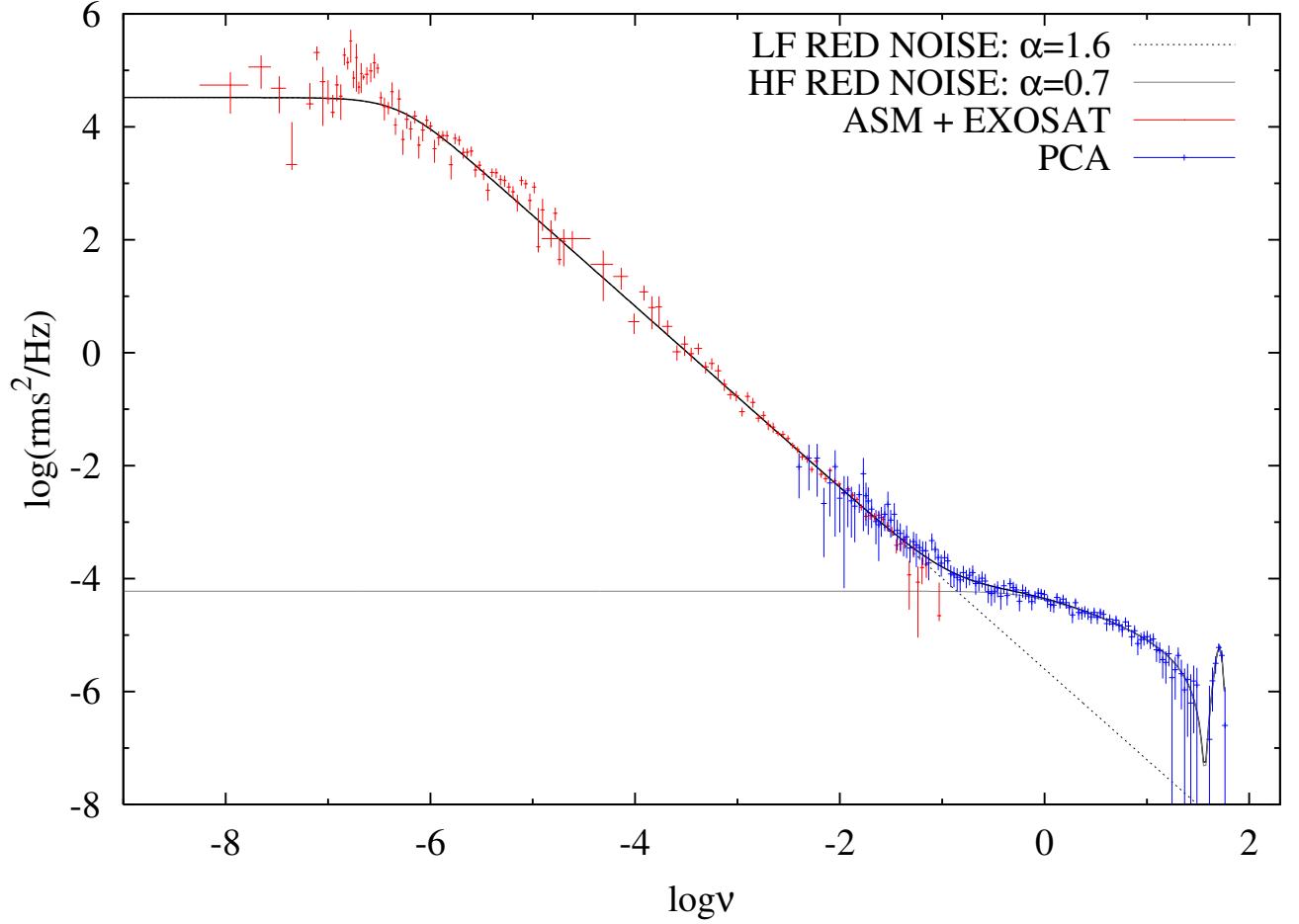


Fig. 11.— EXOSAT-ASM-PCA (RXTE) power spectrum of Cyg X-2 in frequency range that covers 10 orders of magnitude. One can clearly see low and high frequency (LF and HF) white-red noise components in PDS, related to the extended Keplerian disk and relatively compact, inner disk-like configuration (Sub Keplerian Compton cloud) respectively. Each of these two components is perfectly fitted by our white-red noise model (see Eqs. 85 and 86), dotted and solid lines are for LF and HF best-fit models respectively, $\chi^2/N_{dof} = 393.2/244 = 1.6$ (see the text for the best-fit parameters values).

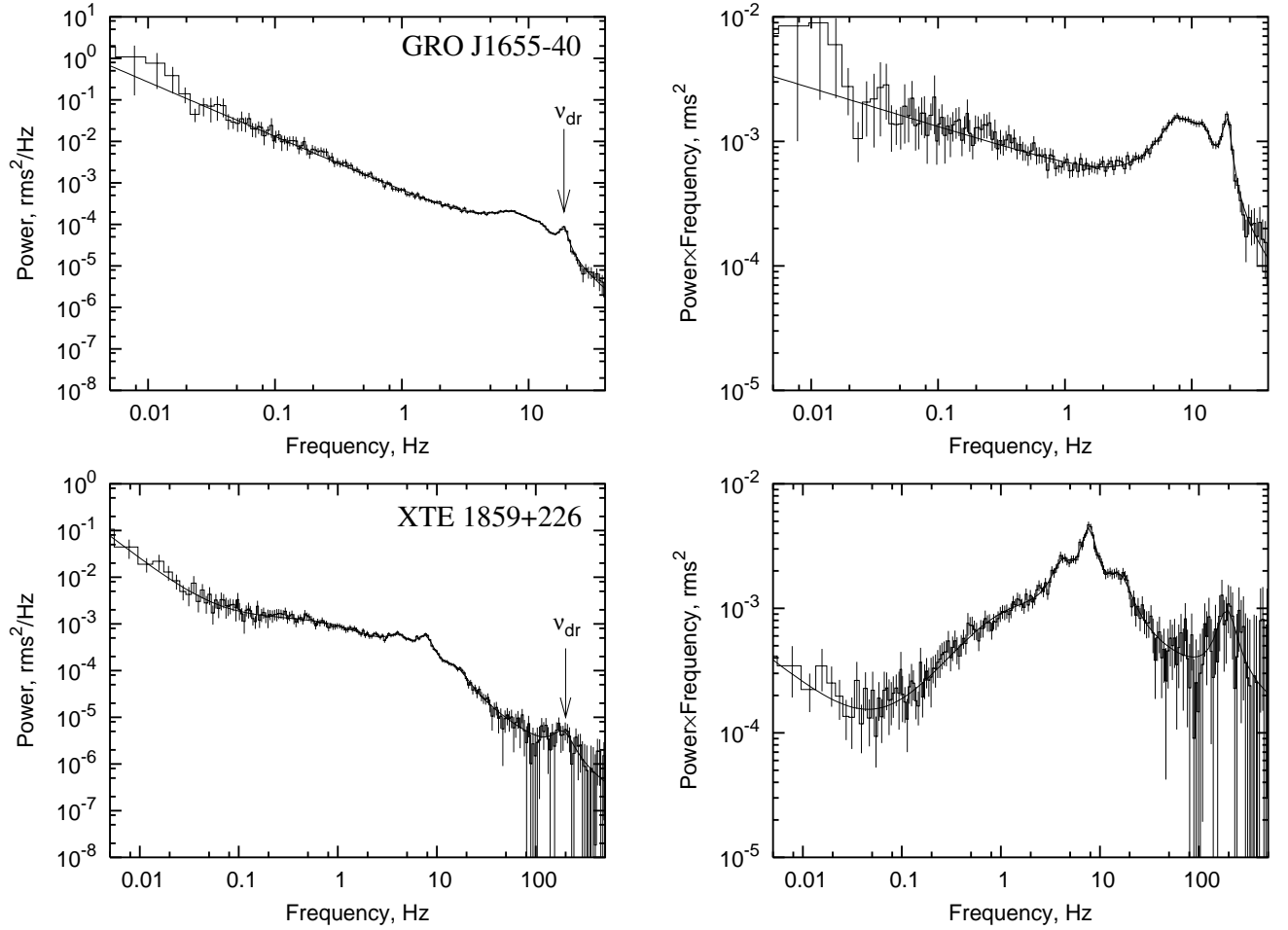


Fig. 12.— RXTE/PCA power spectra (left panels) and power×frequency diagrams (right panels) of GRO J1655-40 (top) and XTE 1859+226 (bottom). One can clearly see QPO frequencies ν_{dr} at $\sim 10 - 20$ Hz for GRO J1655-40 and ~ 185 Hz for XTE 1859+226 before a high-frequency cut-off. The rms^2 power at ν_{dr} is comparable (GRO J1655-40) or higher (XTE 1859+226) than that at low frequencies (see right panels).

Table 1. Summary of RXTE data

Observation ID ^(a)	Date, MJD	ψ_{CC}	$t_{C,0}$, s	ψ_D	t_* , ms	Γ	ν_{QPO} , Hz	χ^2/N_{dof}
10257-01-01-00	50242.1	3.031 ± 0.016	41(3)	$1.017^{+0.030}_{-0.018}$	-	162.0/220
30158-01-03-00	50796.4	2.531 ± 0.070	6.284 ± 1.375	...	13(2)	$0.513^{+0.005}_{-0.002}$	$0.355^{+0.166}_{-0.095}$	96.3/185
40099-01-03-01	51220.3	2.324 ± 0.119	1.793 ± 0.321	...	9(3)	$0.550^{+0.006}_{-0.003}$	$1.240^{+0.144}_{-0.084}$	114.7/213
40099-01-05-00	51251.2	2.067 ± 0.073	1.236 ± 0.116	...	8(2)	$0.648^{+0.005}_{-0.002}$	$1.579^{+0.246}_{-0.128}$	178.7/216
40099-01-19-00	51446.7	1.696 ± 0.093	0.352 ± 0.026	...	5(2)	$0.778^{+0.012}_{-0.010}$	$4.205^{+0.213}_{-0.109}$	147.1/216
40099-01-21-00	51475.7	2.170 ± 0.058	0.644 ± 0.055	...	6(2)	$0.703^{+0.007}_{-0.004}$	$3.318^{+0.208}_{-0.105}$	157.6/216
50109-01-01-00	51900.4	-0.753 ± 0.002	0.034 ± 0.001	2.736 ± 0.076	22(2)	$1.035^{+0.005}_{-0.003}$	-	219.6/217
50109-01-02-03	51904.2	0.105 ± 0.562	0.060 ± 0.013	$0.883^{+0.011}_{-0.006}$	$7.083^{+0.446}_{-0.234}$	153.8/216
50109-01-05-01	51934.0	0.438 ± 0.246	0.061 ± 0.006	1.438 ± 1.062	2(2)	$0.927^{+0.006}_{-0.003}$	$8.703^{+0.207}_{-0.106}$	383.5/214
50110-01-52-00	52385.3	2.937 ± 0.015	106(5)	$1.558^{+0.023}_{-0.011}$	-	252.1/220
50119-01-01-00	51845.6	0.853 ± 0.003	0.045 ± 0.001	2.654 ± 0.106	22(1)	$0.979^{+0.012}_{-0.006}$	-	307.9/189
50119-01-03-02	51851.7	-0.835 ± 0.204	0.038 ± 0.002	1.928 ± 0.805	...	$0.950^{+0.007}_{-0.004}$	$8.363^{+0.339}_{-0.173}$	207.0/186
50119-01-04-01	51897.1	1.632 ± 0.105	0.255 ± 0.023	...	3(2)	$0.810^{+0.007}_{-0.002}$	$4.122^{+0.294}_{-0.152}$	188.1/213
60089-02-01-00	52175.7	3.133 ± 0.011	52(2)	$1.169^{+0.010}_{-0.004}$	-	156.4/220
60089-02-01-01	52175.8	1.696 ± 0.735	0.026 ± 0.009	3.078 ± 0.021	42(4)	$1.138^{+0.008}_{-0.005}$	-	199.6/217
60089-02-02-00	52210.7	1.537 ± 0.107	0.214 ± 0.019	...	2(1)	$0.807^{+0.008}_{-0.005}$	$5.132^{+0.278}_{-0.149}$	186.3/216
60090-01-01-00	52341.2	...	0.052 ± 0.001	2.785 ± 0.051	30(1)	$1.043^{+0.008}_{-0.003}$	-	256.5/217
60090-01-02-00	52358.2	2.801 ± 0.016	52(2)	$1.286^{+0.007}_{-0.003}$	-	213.3/220
60090-01-06-00	52415.1	2.960 ± 0.013	48(2)	$1.248^{+0.013}_{-0.005}$	-	154.1/220
60090-01-07-03	52426.3	3.260 ± 0.014	64(4)	$1.112^{+0.008}_{-0.004}$	-	138.3/220
60090-01-11-01	52481.9	2.845 ± 0.021	90(6)	$1.575^{+0.025}_{-0.009}$	-	172.3/220
60090-01-12-01	52497.9	2.894 ± 0.015	72(4)	$1.493^{+0.022}_{-0.009}$	-	235.4/220
60090-01-12-02	52498.0	3.001 ± 0.021	112(9)	$1.415^{+0.031}_{-0.012}$	-	173.1/220
60090-01-14-01	52524.8	2.967 ± 0.014	57(3)	$1.339^{+0.017}_{-0.011}$	-	203.0/220
60090-01-14-02	52524.9	2.931 ± 0.016	52(3)	$1.298^{+0.017}_{-0.006}$	-	152.7/220
60090-01-14-04	52525.0	3.036 ± 0.014	61(3)	$1.394^{+0.016}_{-0.008}$	-	153.8/220
60090-01-15-01	52537.7	3.073 ± 0.010	41(2)	$1.204^{+0.013}_{-0.006}$	-	149.6/220
60090-01-16-00	52553.7	-0.238 ± 0.228	0.050 ± 0.004	...	6(2)	$0.909^{+0.006}_{-0.003}$	$6.308^{+0.589}_{-0.293}$	241.0/215

Table 1—Continued

Observation ID ^(a)	Date, MJD	ψ_{CC}	$t_{C,0}$, s	ψ_D	t_* , ms	Γ	ν_{QPO} , Hz	χ^2/N_{dof}
60136-03-01-00	52088.2	2.073 ± 0.080	1.098 ± 0.130	$0.583^{+0.007}_{-0.004}$	$2.096^{+0.407}_{-0.216}$	110.4/217
80110-01-12-00	53241.8	2.246 ± 0.063	0.914 ± 0.087	...	7(2)	$0.645^{+0.007}_{-0.004}$	$2.434^{+0.344}_{-0.178}$	133.4/216
80110-01-13-00	53251.7	2.026 ± 0.041	0.547 ± 0.008	...	4(2)	$0.729^{+0.005}_{-0.003}$	$3.955^{+0.220}_{-0.112}$	150.8/216
80110-01-14-00	53267.7	3.073 ± 0.009	49(2)	$1.081^{+0.014}_{-0.004}$	-	203.1/220
80110-01-14-03	53267.9	3.151 ± 0.014	49(3)	$1.107^{+0.007}_{-0.004}$	-	136.6/220
80110-01-15-00	53279.7	...	0.027 ± 0.001	2.961 ± 0.039	32(3)	$1.071^{+0.008}_{-0.007}$	-	238.6/218
80110-01-16-00	53293.7	-0.351 ± 0.565	0.062 ± 0.012	$0.904^{+0.006}_{-0.004}$	$6.687^{+0.444}_{-0.230}$	167.6/215
80110-01-18-00	53321.6	-1.171 ± 0.175	0.128 ± 0.002	3.414 ± 0.322	14(20)	$0.729^{+0.008}_{-0.004}$	$4.287^{+0.263}_{-0.134}$	142.3/214
80110-01-20-04	53352.7	0.825 ± 0.338	0.143 ± 0.022	$0.862^{+0.007}_{-0.004}$	$5.373^{+0.334}_{-0.171}$	166.7/215
80110-01-22-00	53378.5	3.180 ± 0.014	61(4)	$1.249^{+0.020}_{-0.016}$	-	131.1/220
80110-01-23-00	53391.4	1.414 ± 0.126	0.201 ± 0.018	$0.862^{+0.007}_{-0.005}$	$5.568^{+0.228}_{-0.116}$	188.2/216
80110-01-23-04	53391.7	-0.295 ± 0.499	0.067 ± 0.011	$0.901^{+0.008}_{-0.005}$	$6.993^{+0.404}_{-0.209}$	181.3/216